A simulation study of basin water renewal in the Norwegian threshold fjord Haugsværfjorden

Department of Mathematics

University of Bergen

Håvard Mjelde Flo

June 1, 2022

Abstract

In many fjords the renewal of basin water is restricted by topographical barriers called sills. These restrictions may cause the basin water to become stagnant for long periods during which there is no renewal of basin water. During stagnation periods the concentrations of dissolved oxygen will decline which eventually turns the basin water hypoxic unless basin water renewal occurs.

Haugsværfjorden is an example of a threshold fjord with a shallow sill that has hypoxic basin water. In this thesis, three different scenarios of a 10 year simulation of Haugsværfjorden applying dynamic boundary conditions using the Bergen Ocean Model has been done in order to examine the degree of basin water renewal. In the three scenarios the amount of river discharge has been varied and one of the scenarios features a submerged fresh water discharge that is supposed to shorten the stagnation periods.

The model results suggests that there is very little renewal of the basin water and that stagnation periods may last for decades or even longer. However, even during stagnation periods partial renewal of the intermediate layer in the fjord is seen. The model results shows that intruding water masses must be significantly more dense than the basin water in order to renew the deepest basin water. The exact amount denser the intruding water must be depends on local factors as for instance the topography, but in Haugsværfjorden the intrusions were typically 0,5 % more dense that the basin water before basin water renewal occurred.

Acknowledgements

First and foremost, I would like to thank my supervisor, Jarle Berntsen, for his guidance. You are always happy to help your students when they are in need, and you have kept me motivated and inspired through many interesting conversations. I would also like to thank my fellow student, Erlend Mundal, for the cooperation and sharing the experience.

My wife was the person who originally motivated me to write my master's thesis, which I have not regretted for a second, so she deserves some of the credit for this thesis. To my beloved Audrey: Thank you very much for believing in me.

My family and close friends have all supported in so many different ways. Thank you, all.

Contents

Chapter 1

Introduction

Fjords can be found around the world in areas of previous glacial activity. They were carved out by glaciers and have since been filled with ocean water. Fjords are commonly very long and narrow and are often situated between tall steep mountains whose slopes continue below the surface of the fjord making the fjords quite deep. In fact, fjords can often be deeper than the surrounding continental shelf at the coast (Farmer and Freeland (1983)).

Since fjords contains oceanic water and receives considerable amount of fresh water discharge from rivers especially at the head of the fjord, they can be characterised as an estuary (Farmer and Freeland (1983)). The fresh water discharge from rivers makes parts of the fjord brackish (Aksnes et al. (2019)). Throughout the fjord and especially at the mouth there is continuous mixing of brackish fjord water and oceanic water. The nature of this mixing greatly depends on the topography of the fjord.

Commonly, fjords have one or more sills, often one at the mouth. Fjords that have one or more sills are called threshold fjords. A sill is a significantly more shallow, and sometimes more narrow, section of the fjord constricting the fluid flow over the sill. The fjord basin is the portion of the fjord inside the sill below the sill depth. The water that occupies the fjord basin is called the basin water. The constriction at the sill may severely restrict the coastal water from entering the fjord thus reducing the renewal of the basin water. Fjords tend to have a strong stratification due to the large amount of fresh water discharged into the fjord surface which causes the surface layer of the fjord to have a significantly lower salinity than the deeper layers of the fjord. The basins of fjords are normally occupied by the most dense water which have entered the fjord at some point in time, which may very well be coastal or oceanic water. Thus, the basin water may have the same salinity and temperature as deep oceanic water, hence the large density difference between the layers of the fjord (Stigebrandt and Aure (1989)).

All water entering the fjord must flow over the sill. If the density of the entering water masses are greater than the density of the basin water, ρ_b, the entering

water sinks into the basin. Such an event is called a high density intrusion (Aksnes et al. (2019)). Since the density of the basin water is commonly of comparable size with the density of coastal water, high density intrusions are quite rare in some fjords (Aksnes et al. (2019)). The oxygen consumption in the basin water due to biological activity is typically larger than the supply of oxygen caused by diffusion alone (Aksnes et al. (2019)). Thus, when there is an absence of high density intrusions over an extended period of time a stagnation period starts and the amount of dissolved oxygen in the basin water will decline. This will eventually lead to hypoxic, and in some cases anoxic, conditions, which limits what life forms can survive in the basin water (Stigebrandt and Aure (1989)).

Recent studies have examined how a rising temperature of the ocean will impact the frequency of high density intrusions in threshold fjords. Aksnes et al. (2019) have studied Masfjorden and found that the dissolved oxygen in the basin water has decreased in the last 50 years, possibly due to a lowered frequency of high density intrusions in Masfjorden. Aksnes et al. (2019) points out that the decline in the frequency of high density intrusions seen in Masfjorden probably has occurred in other fjords in the area as well. The basin volume of Masfjorden is considered large and according to Aksnes et al. (2019) the stagnation period must be around 7-12 years in order to make the basin water in Masfjorden anoxic. The long required stagnation period and deep sills of Mafjorden might suggest that Masfjorden is quite resilient, and will rarely or never turn anoxic. According to Darelius (2020) the probability of a 7 year stagnation period in Masfjorden is 28%. However one of the assumptions for this calculation is that whenever the density of the water at sill depth, ρ_s, is greater than or equal ρ_b, a complete renewal, or displacement, of the basin water will occur. Most intrusions events in the model are expected to only partially displace the basin volume, thus the approximated probability of a 7 year stagnation period may be too great.

One of the sidearms to Masfjorden is Haugsværfjorden. The depth of the sill at the mouth of Haugsværfjorden is only 9 m which can be considered very shallow. When the depth of the sill is very shallow, as in Haugsværfjorden, it is expected to greatly impact the probability of basin water renewal. Thus the stagnation periods are probably very long, possibly leading to hypoxic conditions in the basin water. Additionally, the fact that the sill is very shallow might give rise to other limiting factors such as hydraulically controlled flow over the sill. Thus, if the flux of the water flowing out of over the sill is great enough the inflow might stop due to the excessive flow out over the sill. River discharge at the fjord head will for instance induce a flux out over the sill, and if this flux is large enough, hydraulic control might arise over the sill.

Hypoxic conditions in Haugsværfjorden, and other fjords, will greatly restrict both the life in the fjords but also the productivity in the fjord. Aksnes et al. (2019) included the impact of fish farming on the oxygen consumption in the model of Masfjorden. A globally decreasing concentration of the dissolved oxygen in fjords makes the dynamic systems of the fjord vulnerable to the increased oxygen consumption caused by for instance fish farms in the fjord. The trend of decreasing dissolved oxygen concentrations in fjords is a good motivation for

understanding the renewal of basin water in threshold fjord.

In this thesis, Haugsværfjorden will be examined in three different scenarios. Specifically, the main topic is to study how the renewal of basin water is impacted by varying river discharges and a submerged fresh water discharge. In the three scenarios that are studied the parameters are changed according to the tabular below.

Scenario no.	Flux of river M	Flux of river H	Submerged discharge
1	155 m^3/s	10 m^3/s	0 m^3/s
2	0 m^3/s	0 m^3/s	0 m^3/s
3	155 m^3/s	10 m^3/s	0.5 m^3/s

In the model there are two river discharges, one is at the head of Matresfjorden and the other is at the head of Haugsværfjorden which corresponds to river M and river H in the tabular above, respectively. In the first scenario the river fluxes are set at realistic constant values. Since the river fluxes are constant, seasonal changes in the river discharge is omitted from the model. However, there is extensive hydropower production in Matresfjorden which is a source of constant river discharge through the winter season, which would normally be a period in the year with very low river discharges. In reality, the discharge from rivers is probably lowest during dry periods in the summer season, but this is omitted from the model completely.

In the second scenario has no river discharge at all. All movement of the fluid in the second scenario is driven by the dynamic boundary conditions at the outer boundary. The results of this scenario will hopefully reveal some of the dynamics at the sill, considering that the constricting constant outflow of brackish surface water is absent.

In the third scenario the effects of a submerged fresh water discharge on the renewal of basin water is studied. The idea is that releasing fresh water at the basin floor will shorten the stagnation periods in the basin thus increasing the frequency of basin water renewal.

In order to study these scenarios the σ-coordinate numerical ocean model Bergen Ocean Model (BOM) as described by Berntsen (2004) has been used. The following chapters will describe the equations used in BOM and the domain on which it is applied in addition to the results of the study that will be presented an discussed.

Chapter 2

Equations of Motion

The equation used in Bergen Ocean Model is the Reynolds averaged Navier-Stokes equations for an incompressible flow using the Boussinesq approximation. Furthermore, the fluid is assumed to be in hydrostatic balance. This model is explained in Cushman-Roisin and Beckers (2011) among many other places. The following chapter describes the equations used in BOM according to Berntsen (2004).

2.1 Governing equations

The continuity equation for an incompressible fluid is

$$\frac{\partial U}{\partial x} + \frac{\partial V}{\partial y} + \frac{\partial W}{\partial z} = 0 \tag{2.1.0.1}$$

where U, V and W is the fluid velocity in the x, y and z-direction, respectively. The the momentum equations are

$$\frac{\partial U}{\partial t} + U\frac{\partial U}{\partial x} + V\frac{\partial U}{\partial y} + W\frac{\partial U}{\partial z} - fV = -\frac{1}{\rho_0}\frac{\partial P}{\partial x} + \frac{\partial}{\partial z}\left(K_M\frac{\partial U}{\partial z}\right) + F_x \tag{2.1.0.2}$$

$$\frac{\partial V}{\partial t} + U\frac{\partial V}{\partial x} + V\frac{\partial V}{\partial y} + W\frac{\partial V}{\partial z} + fU = -\frac{1}{\rho_0}\frac{\partial P}{\partial y} + \frac{\partial}{\partial z}\left(K_M\frac{\partial V}{\partial z}\right) + F_y \tag{2.1.0.3}$$

$$\rho g = -\frac{\partial P}{\partial z} \tag{2.1.0.4}$$

Here f is the Coreolis parameter, P is pressure, g is the gravitational acceleration, ρ is density and ρ_0 is the reference density from the Boussinesq approximation. In this study the Coriolis effect is assumed negligible, thus $f = 0$. The

momentum diffusion has been split in vertical and horizontal terms where K_M is the vertical viscosity, and F_x and F_y represents the sub-grid scale mixing due to the horizontal viscosity. The simplification due to the hydrostatic approximation allows the pressure, P, to be obtained by integrating equation (2.1.0.4) from z to the surface elevation, η

$$P(x, y, z, t) = P_{\text{atm}} + g\rho_0\eta + g\int_z^0 \rho(x, y, Z)dZ \tag{2.1.0.5}$$

P_{atm} is the atmospheric pressure and is assumed constant. The equations describing the transport of salinity and temperature can be written as

$$\frac{\partial T}{\partial t} + U\frac{\partial T}{\partial x} + V\frac{\partial T}{\partial y} + W\frac{\partial T}{\partial z} = \frac{\partial}{\partial z}\left(K_H\frac{\partial T}{\partial z}\right) + F_T \tag{2.1.0.6}$$

$$\frac{\partial S}{\partial t} + U\frac{\partial S}{\partial x} + V\frac{\partial S}{\partial y} + W\frac{\partial S}{\partial z} = \frac{\partial}{\partial z}\left(K_H\frac{\partial S}{\partial z}\right) + F_S \tag{2.1.0.7}$$

where T is the temperature and S is the salinity. The equation describing the transport of oxygen is quite similar to the equations 2.1.0.6 and 2.1.0.7 but involves the term $-b$ denoting the consumption of oxygen due to biological processes. The equation for transport of oxygen is as follows

$$\frac{\partial O_2}{\partial t} + U\frac{\partial O_2}{\partial x} + V\frac{\partial O_2}{\partial y} + W\frac{\partial O_2}{\partial z} = \frac{\partial}{\partial z}\left(K_H\frac{\partial O_2}{\partial z}\right) + F_{O_2} - b \tag{2.1.0.8}$$

Here K_H denotes the vertical diffusivity of heat, salt and oxygen. F_T, F_S and F_{O_2} denotes sub-grid scale horizontal diffusion of heat, salt and oxygen respectively. In the model, the density depends only on the temperature and salinity and an equations of state of the form

$$\rho = \rho(S, T) \tag{2.1.0.9}$$

can be formulated. The specific equation used in this model is the equation of state used by Wang (1984):

$$\sigma_t = 28.152 - 0.0735T - 0.00469T^2 + (0.802 - 0.002T)\,(S - 35) \tag{2.1.0.10}$$

$$\rho = 1 + \sigma_t \cdot 10^{-3} \tag{2.1.0.11}$$

The terms describing viscosity and diffusion has been split into horizontal and vertical components. This is due to the fact that there is a large difference in the magnitude of the unresolved processes. The vertical resolution is much

higher than the horizontal resolution, therefore the difference in magnitudes of the corresponding viscosity and diffusion terms are large and they must be dealt with separately.

The horizontal viscosity terms, F_x and F_y, are calculated as follows

$$\begin{aligned} F_x &= \frac{\partial}{\partial x}\left(A_M \frac{\partial U}{\partial x}\right) + \frac{\partial}{\partial y}\left(A_M \frac{\partial U}{\partial y}\right) \\ F_y &= \frac{\partial}{\partial x}\left(A_M \frac{\partial V}{\partial x}\right) + \frac{\partial}{\partial y}\left(A_M \frac{\partial V}{\partial y}\right) \end{aligned} \tag{2.1.0.12}$$

and acts as a diffusion of the momentum in the fluid. The horizontal diffusion terms, F_T, F_S and F_{O_2}, are

$$\begin{aligned} F_T &= \frac{\partial}{\partial x}\left(A_H \frac{\partial T}{\partial x}\right) + \frac{\partial}{\partial y}\left(A_H \frac{\partial T}{\partial y}\right) \\ F_S &= \frac{\partial}{\partial x}\left(A_H \frac{\partial S}{\partial x}\right) + \frac{\partial}{\partial y}\left(A_H \frac{\partial S}{\partial y}\right) \\ F_{O_2} &= \frac{\partial}{\partial x}\left(A_H \frac{\partial O_2}{\partial x}\right) + \frac{\partial}{\partial y}\left(A_H \frac{\partial O_2}{\partial y}\right) \end{aligned} \tag{2.1.0.13}$$

The diffusivities, $A_M = 450.0$ and $A_H = 0$, are constant in time and space

2.2 Vertical Mixing

The vertical viscosity, K_M, and the vertical diffusivity, K_H, needs to be determined to close the system of equations above. The turbulence closure scheme described here is the Mellor and Yamada $2\frac{1}{2}$ level model
(Mellor and Yamada (1982)). The governing equations for turbulent kinetic energy, $q^2/2$, and a turbulence macroscale, l, are given by

$$\begin{aligned} &\frac{\partial q^2}{\partial t} + U\frac{\partial q^2}{\partial x} + V\frac{\partial q^2}{\partial y} + W\frac{\partial q^2}{\partial z} = \frac{\partial}{\partial z}\left(K_q \frac{\partial q^2}{\partial z}\right) \\ &+ 2K_M\left(\left(\frac{\partial U}{\partial z}\right)^2 + \left(\frac{\partial V}{\partial z}\right)^2\right) + \frac{2g}{\rho_0}K_H\frac{\partial \rho}{\partial z} - \frac{2q^3}{B_1 l} \end{aligned} \tag{2.2.0.1}$$

and

$$\frac{\partial q^2 l}{\partial t} + U\frac{\partial q^2 l}{\partial x} + V\frac{\partial q^2 l}{\partial y} + W\frac{\partial q^2 l}{\partial z} = \frac{\partial}{\partial z}\left(K_q \frac{\partial q^2 l}{\partial z}\right) + lE_1 K_M \left(\left(\frac{\partial U}{\partial z}\right)^2 + \left(\frac{\partial V}{\partial z}\right)^2\right) + \frac{lE_1 g}{\rho_0} K_H \frac{\partial \rho}{\partial z} - \frac{q^3}{B_1 l}\tilde{W} \tag{2.2.0.2}$$

The turbulence closure scheme balances the forces of the vertical velocity shear and the stratification. Thus, the turbulent mixing in the model is proportional to the vertical velocity shear and the vertical density gradient. For instance, a large vertical velocity shear and a very small vertical density gradient corresponds to a low Richardson number. If the Richardson number is less then 1/4 the forces of turbulence overcomes the stratification in the fluid and turbulent mixing arises. However, a negative density gradient, which is commonly seen in stratified fluids, will limit the amount turbulent mixing, thus preventing layers of different density in a fluid from mixing. There might occur instances when $\partial\rho/\partial z > 0$ which will dramatically increase the turbulent mixing. This might for instance occur if a fluid parcel sits above another fluid parcel of lower density. In that case, the two parcels will turbulently mix creating a new parcel which is a mix of the two previous parcels. $\tilde{W}$ is a function defined as

$$\tilde{W} = 1 + E_2 \left(\frac{l}{\kappa L}\right)^2 \tag{2.2.0.3}$$

and L^{-1} is defined by

$$L^{-1} = (\eta - z)^{-1} + (H + z)^{-1} \tag{2.2.0.4}$$

$\kappa = 0.4$ is the von Karman constant. According to Blumberg and Mellor (1987) the mixing coefficients K_M, K_H and K_q can be described by the following expressions

$$\begin{aligned} K_M &= lqS_M \\ K_H &= lqS_H \\ K_q &= lqS_q \end{aligned} \tag{2.2.0.5}$$

Where S_M, S_H and S_q are stability functions. The mixing coefficients are seen to be proportional to the turbulence and the turbulent length scale. Thus, an increase in turbulent mixing is a positive feedback loop reinforcing itself. However, in a stratified fluid the turbulence and the turbulence length scale will always tend towards zero assuming the vertical velocity shear is not very large. Defining

$$G_H = \frac{l^2}{q^2}\frac{g}{\rho_0}\frac{\partial \rho}{\partial z} \tag{2.2.0.6}$$

The stability functions become

$$
\begin{aligned}
&S_H\left(1-\left(3A_2B_2+18A_1A_2\right)G_H\right)=A_2\left(1-6\frac{A_1}{B_1}\right)\\
&S_M\left(1-9A_1A_2G_H\right)-S_H\left(\left(18A_1^2+9A_1A_2\right)G_H\right)=A_1\left(1-3C_1-6\frac{A_1}{B_1}\right)\\
&S_q=0.20
\end{aligned}
\tag{2.2.0.7}
$$

According to Mellor and Yamada (1982) the values
$A_1, A_2, B_1, B_2, C_1, E_1, E_2$ are assigned the values

$$
(A_1, A_2, B_1, B_2, C_1, E_1, E_2) = (0.92, 0.74, 16.6, 10.1, 0.08, 1.8, 1.33) \tag{2.2.0.8}
$$

2.3 Boundary Conditions

The surface of the fjord is a free surface, so at $z = \eta(x, y)$

$$
\begin{aligned}
\rho_0 K_M\left(\frac{\partial U}{\partial z},\frac{\partial V}{\partial y}\right)&=(\tau_{0x},\tau_{0y})\\
\rho_0 K_H\left(\frac{\partial T}{\partial z},\frac{\partial S}{\partial z},\frac{\partial O_2}{\partial z}\right)&=\left(\dot{T}_0,\dot{S}_0,\dot{O}_{20}\right)\\
q^2&=B_1^{2/3}u_{\tau s}\\
l&=0
\end{aligned}
\tag{2.3.0.1}
$$

where $u_{\tau s}=\left(\vec{\tau_0}^{\,2}\right)^{1/2}$. (τ_{0x}, τ_{0y}) is the wind stress at the surface, and $\left(\dot{T}_0, \dot{S}_0, \dot{O}_{20}\right)$ is the heat flux, the evaporation and the oxygen exchange at the surface, respectively. In this model the wind stress is always at zero and the fluxes of heat, salt and oxygen is zero through the surface, bottom and side walls. The vertical velocities at the surface and the bottom are given by

$$
\begin{aligned}
W_0&=U\frac{\partial\eta}{\partial x}+V\frac{\partial\eta}{\partial y}+\frac{\partial\eta}{\partial t}\\
W_b&=-U_b\frac{\partial H}{\partial x}-V_b\frac{\partial H}{\partial y}
\end{aligned}
\tag{2.3.0.2}
$$

The bottom drag on the horizontal velocities are given by

$$\rho_0 K_M \left(\frac{\partial U}{\partial z}, \frac{\partial V}{\partial y} \right) = (\tau_{bx}, \tau_{by}) \tag{2.3.0.3}$$

The stress at the bottom is given by

$$\vec{\tau}_b = \rho_0 C_D |\vec{U}_b| \vec{U}_b \tag{2.3.0.4}$$

where the drag coefficient, C_D, is given by

$$C_D = \max \left[0.0025, \frac{\kappa^2}{\left(\ln \left(z_b / z_0 \right) \right)^2} \right] \tag{2.3.0.5}$$

Here z_b is the distance from the bottom to the nearest grid point. The bottom roughness parameter, z_0, is assigned the value $z_0 = 0.01$ m. At the bottom the conditions for q^2 and l are

$$\begin{aligned} q^2 &= B_1^{2/3} u_{\tau b} \\ l &= 0 \end{aligned} \tag{2.3.0.6}$$

where $u_{\tau b} = \left(\vec{\tau_b}^2 \right)^{1/2}$.

The set of equations described thus far form set of simultaneous partial differential equations with no known analytic solutions. Therefore, the equations are discretized and solved numerically using the Bergen Ocean Model described by Berntsen (2004).

Chapter 3

The Masfjorden Fjord System

The fjord system studied in this thesis is the Masfjorden fjord system with a particular focus on Haugsværfjorden which is a small and partially isolated part of the fjord system. The location of the system is in the south-west of Norway and can be seen in the map in figure 3.1.

The mouth of the Masfjorden fjord system is around 40 km from the North Sea along the waterways. The North Sea is the closest open ocean to Masfjorden, but Masfjorden is not directly connected to it. However, Masfjorden is connected to the deep fjord Fensfjorden which is directly connected to the North Sea. Fensfjorden is more than 500 m deep in large portions of the fjord, and is even deeper than 650 m outside the mouth Masfjorden. The North Sea is significantly more shallow than Fensfjorden, thus Fensfjorden has a basin itself. However, the sill depth of Fensfjorden is significantly deeper than the sill depth of Masfjorden and the ventilation of Fensfjorden is assumed to be no limitation on the system. In figure 3.2 the location of the Masfjorden fjord system relative to Fensfjorden and The North Sea is presented.

In figure 3.2 the location of the permanent hydrographical station in Sognesjøen is also displayed. Sognesjøen is a fjord that, in a similar way to Fensfjorden, is directly connected to The North Sea. The permanent station in Sognesjøen has measured salinity, temperature and density at approximately a 14 day frequency since 1935. Such extensive measurements are not available for Fensfjorden. Thus, the measurements from Sognesjøen will be used to approximate the state of Fensfjorden at a given point in time after 1935. In the model the state of Fensfjorden is represented as the boundary conditions at the mouth of the Masfjorden system.

In figure 3.3 a more detailed view of the Masfjorden fjord system is shown. As mentioned, the Masfjorden system borders to Fensfjorden at the mouth of Masfjorden. Inside the mouth of Masfjorden there is a pool of water situated

Figure 3.1: The location of Masfjorden in southern Norway. The map is collected from Kartverket (2022)

outside the outer sill of the system. In this pool the depth varies a lot, but there is a valley along the bottom topography where the depth is always larger than 100 m, and mostly deeper than 150 m. In the model this pool has a constant depth of 150 m. The outer sill of Masfjorden has a minimum depth of 68 m, while inside of this sill there is a basin reaching depths of nearly 300 m. The inner sill of Masfjorden has a minimum depth of 196 m. Inside of the inner sill the deepest basin of Masfjorden is found which reaches a maximum depth of 486 m. In the inner part of Masfjorden, the system divides into two fjords. The part stretching eastward is called Matresfjorden and is a more shallow extension of the inner basin of Masfjorden with no sill at the mouth, and the part stretching north-eastward is Haugsværfjorden.

Matresfjorden is, as mentioned, a shallower extension of Masfjorden. At different locations along Matresfjorden a substantial amount of fresh water runs into the

Figure 3.2: In this figure the location of the Masfjorden fjord system is outlined by the dashed black line. The point in the north of the figure is the permanent hydrographic station at Sognesjøen. The map is collected from Kartverket (2022).

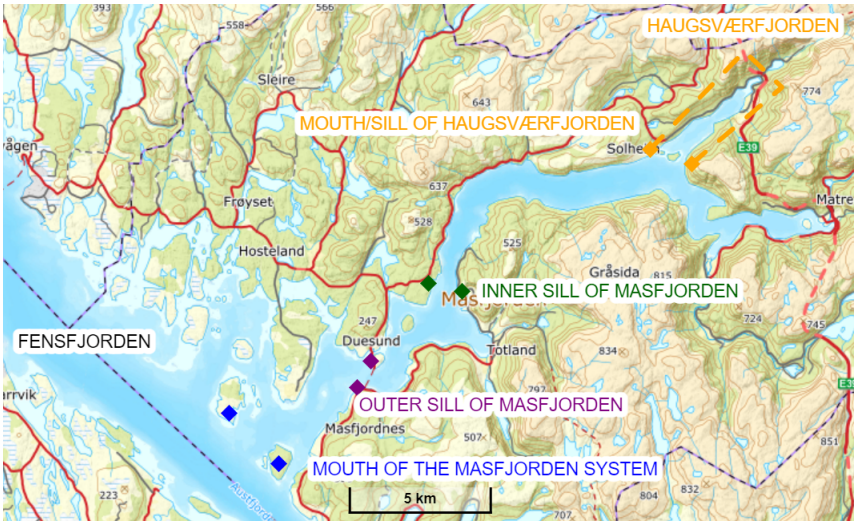

Figure 3.3: An overview of the Masfjorden fjord system. The boundary between the fjord system and Fensfjorden is located between the blue squares. Similarly the two sills in Masfjorden are marked in purple and green. The mouth and sill of Haugsværfjorden is marked in orange, with a dashed orange line around Haugsværfjorden. The map is collected from Kartverket (2022).

fjord. There are also several large hydroelectrical power plants that pours water into the fjord. Thus, there is a large amount of fresh water running into the fjord throughout the whole year. This fresh water discharge greatly affects the salinity, and thus the density, of the surface water in the fjord system.

The sill in Haugsværfjorden is, as mentioned, very shallow. In the sound where the sill is located, there is an island called Solheimsøyna which can be seen in figure 3.4. Solheimsøyna divides the inlet to Haugsværfjorden into two inlets located west and east of Solheimsøyna. As such, water can enter and exit the fjord in both inlets. In the model, Solheimsøyna is completely removed and the sill at the inlet has a constant depth of 9 m. This is the depth of the small submerged elevation in the inlet east of Solheimsøyna which is seen in figure 3.4 and it is assumed that 9 m is the appropriate depth of the sill in the model.

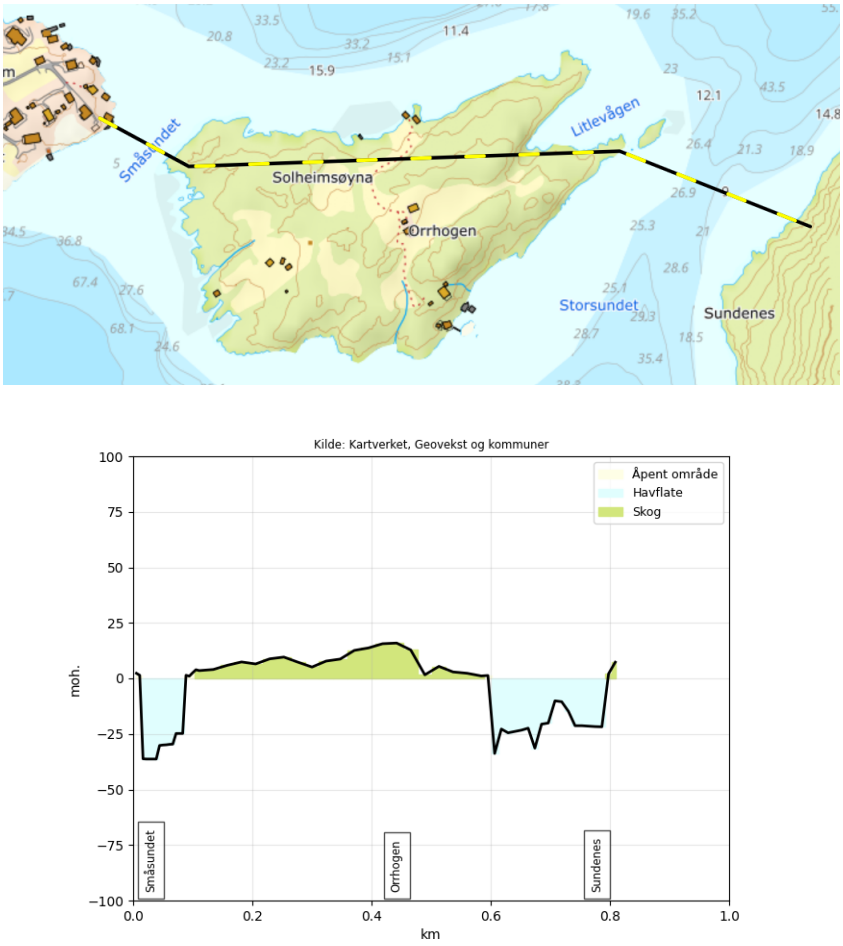

Figure 3.4: The upper image displays a detailed view of the mouth of Haugsværfjorden, while the lower image shows the profile of the elevation along the black and yellow line from the upper image Kartverket (2022).

The maximum depth of the basin in Haugsværfjorden is significantly deeper

than the sill, reaching a depth of around 120 m. Since the sill into Haugsværfjorden is very shallow compared to the sill into Masfjorden it is reasonable to believe that the dynamics of these two fjords are very different even though they are connected. At 68 m depth, which is the depth of the outer sill in Masfjorden, the vertical velocity shear throughout the water column in a two-way flow situation is not expected to be very large. However, in Haugsværfjorden the vertical velocity shear in a two-way flow over the sill in Haugsværfjorden is most likely significantly larger than over the sill in Masfjorden, thus reducing the maximum transport capacity over the sill. Considering that there is a more or less continuous transport of river discharge out over the sill of Haugsværjforden, the probability of an intrusion into the basin is quite low.

However, dense water most definitely has entered Haugsværfjorden at some point in time, which is evident from the measurements provided by Havforskningsinstituttet seen in figure 3.5. According to these measurements the basin water of Haugsværfjorden is hypoxic and high in salinity.

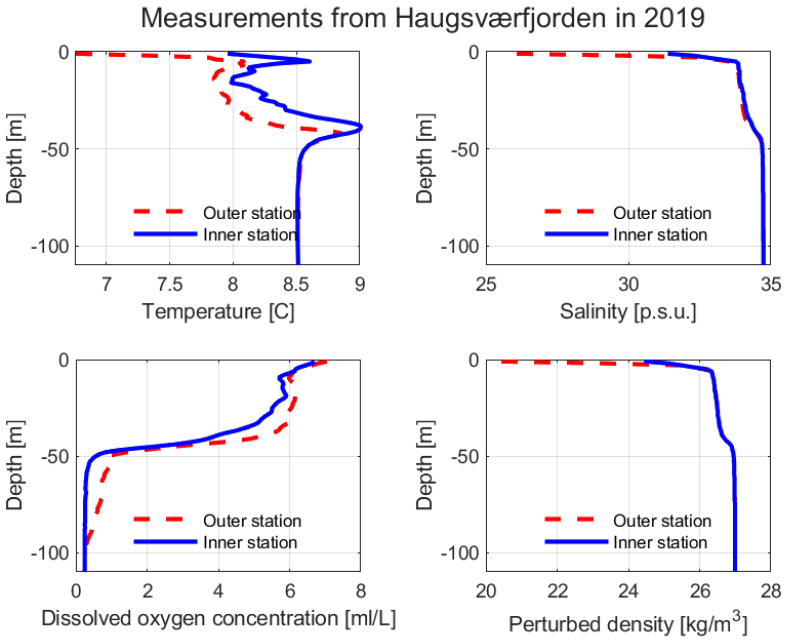

Figure 3.5: Measurements from the basin of Haugsværfjorden at 28. February 2019

The perturbed density, ρ', referred to in figure 3.5 is defined as

$$\rho' = \rho - 1000 \tag{3.0.0.1}$$

where ρ the density.

The water column at the basin can roughly be divided into two parts: above

and below the pycnocline and thermocline which is observed at around 40-50 metres depth. Above the pycnocline the salinity decreases as the surface is approached. The surface layer is thus constituted of brackish water. The lowest temperatures in the water column are found in the surface layer, which is typical for the winter season. During summers it is normally reversed. Above the pycnocline the fjord has a higher concentration of dissolved oxygen than below it, which suggests that the water above the pycnocline is well ventilated.

Below the pycnocline the temperature, salinity and density stabilizes at around 8.5 C, 34 p.s.u. and 1027 kg/m^3, respectively. The concentration of dissolved oxygen changes drastically inside the pycnocline and is nearly zero below the pycnocline. Thus, the basin water in Haugsværfjorden is hypoxic at the time depicted in the figure 3.5.

The salinity of the basin water is considered high and is similar to that of coastal or oceanic water. Thus, high density intrusions do occur in Haugsværfjorden bringing coastal or oceanic water into the basin. However, the hypoxia of the basin water suggests that the stagnation periods are very long and that the intrusions only partly renew the basin water. If the stagnation periods are sufficiently long, the basin water turns hypoxic before intrusions renew the basin water. Additionally, the extent of the renewal of basin water depends on the volume of the high density intrusion and thus the duration of the intrusion. In principle a high density intrusion of a large volume will displace an equally large volume of basin water. However, if the flux into the basin is too large, the flow might stop at the sill due to hydraulic control. Thus, a high density intrusion of high volume must gradually enter the basin.

A suspected effect of a high density intrusion into Haugsværfjorden is ventilation of the basin water and an elevation of the pycnocline. The amount of ventilation of the basin water will be according to the volume of the intrusion. The pycnocline is deep relative to the sill, and since a high density intrusion will sink along the fjord floor, the basin volume beneath the pycnocline will increase. Since the basin water will not exit the fjord a high density intrusion leads the less dense water from above the pycnocline to leave the fjord.

Most natural dynamic systems are in a state of equilibrium, and the same can be assumed for Haugsværfjorden. Thus, the hypoxia of the basin water is most likely a common scenario in Haugsværfjorden. However, events that will change this state momentarily may arise. Nevertheless, the basin water in Haugsværfjorden might in fact have been hypoxic for a very long time.

In the chapter above, the area in which Haugsværfjorden is situated has been described. In the next chapter the model of this fjord system is described.

Chapter 4

The model set up

In all three simulated scenarios in this thesis, the simulated period has been 10 years starting the 1st of January 2012. The domain and initial values are the same in every scenario, while the boundary conditions are changing. The model set up will be described in this chapter.

4.1 The Domain

The domain of the model is seen in figure 4.1

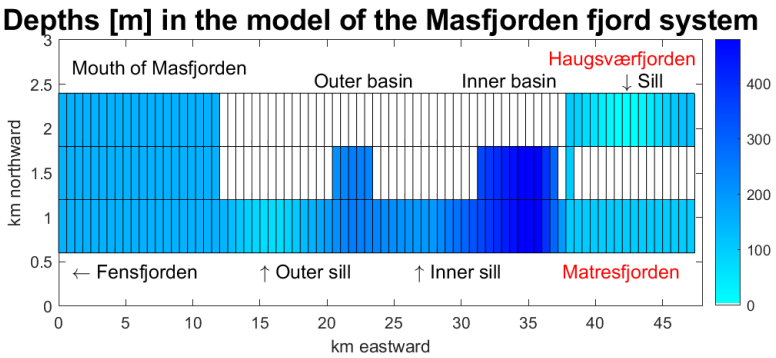

Figure 4.1: A view from above of the model of the Masfjorden fjord system. The white rectangles are land, and the blue ones are the fjord. The length scale in the eastward direction in this figure is compressed, and each cell is actually 600m×600m in the horizontal.

The domain spans 3 km in the north-south direction and 48 km in the east-west direction. The fjord is surrounded by land on all sides except at the western open boundary which is the only part of the model where there are fluxes out of the boundary.

The topography of the fjord floor is constructed using the depths of the three sills and the maximum depth of the three basins. At the sills and in the basins all cells attain the sill depth or basin depth, and in the cells between sills and basins a linear slope is constructed. The depth outside the outer sill and the depth of Matresfjorden is set constant at 150m and 100m, respectively. In order to avoid small scale numerical noise a first order Shapiro filter is applied to smooth out rough edges in the bottom topography (Berntsen (2004)). The Shapiro filter recalculates the depth, H, of a cell with coordinates (i, j) according to

$$H_{\text{new}}(i,j) = \frac{1}{4}\left(H(i-1,j) + 2H(i,j) + H(i+1,j)\right)$$

where i is the cell number in the eastward direction, and j is the cell number in the northward direction.

In figure 4.1 it can be seen that Masfjorden and Matresfjorden are approximated as straight fjords. This approximation is made to avoid a separation of flow around sharp edges and the excessive mixing related to separation of the flow. The physical mixing processes due to irregularities in the actual fjord bank can be represented as friction in the model in stead. In both basins of Masfjorden the fjord spans 2 cells in the north-south direction in order to achieve the correct basin volume in the model.

Haugsværfjorden is connected to Masfjorden and Matresfjorden through a single cell which has a depth of 100 metres. Haugsværfjorden is also straight in the model. In contrast to Masfjorden, Haugsværfjorden is rather straight in reality, which can be seen in figure 3.3. In the model, Haugsværfjorden including the part outside the sill consists in total of 16 cells. Inside the sill there are 7 cells, which corresponds to a length of 4,2 km.

4.2 Initial Values

The initial values are based on measurements from Masfjorden in 2011 and Haugsværfjorden in 2019. The measurements from Masfjorden initiates the field variables in all cells except the cells inside the sill of Haugsværfjorden. The field variables in the cells inside Haugsværfjorden are initiated using the measurements from Haugsværfjorden. The data from Haugsværfjorden is not consistent with the starting date of the model, but the data from 2019 are the earliest data available. The data used can be seen in figure 4.2 and 4.3.

The plots seen in figure 4.2 and 4.3 are vertical profiles of the four field variables temperature, dissolved oxygen, salinity and perturbed density at the deepest points of each fjord. Both vertical profiles exhibits similar features. The vertical profiles of Masfjorden can roughly be divided into two parts: below and above around 100 m. Above 100 m depth all four variables changes with varying depth characteristic of a stratified fluid. In the upper 100 m the pycnocline, thermocline and halocline are seen. The surface layer of Masfjorden is brackish

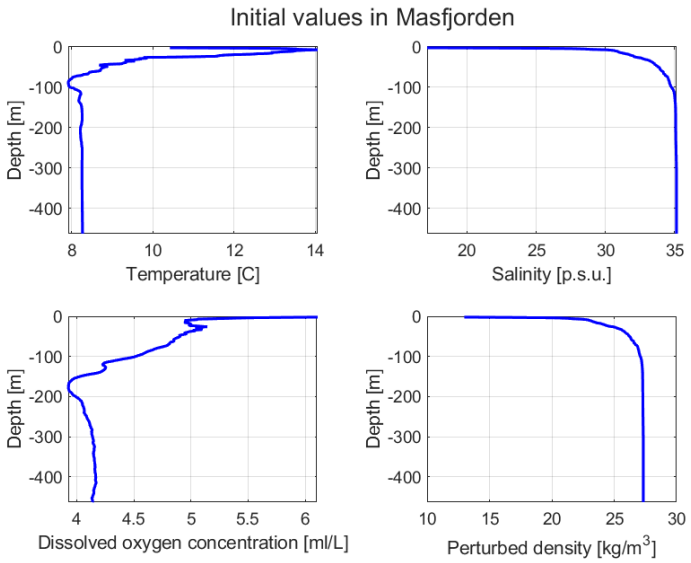

Figure 4.2: The state of the Masfjorden basin in 2011 prior to the start of the simulation period.

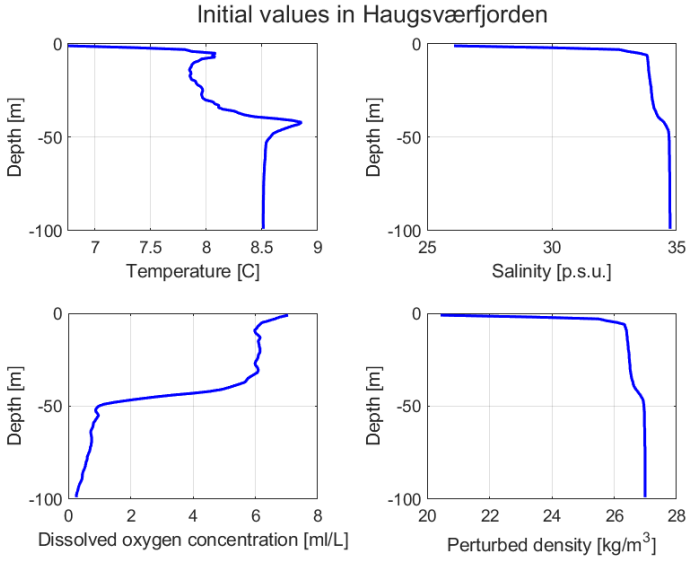

Figure 4.3: The state of the Haugsværfjorden basin in 2019.

due to river discharging into the surface layer, which is typical in fjords. Below 100 m the four variables are nearly constant, characteristic of homogeneous basin water. The data seen from Masfjorden is clear evidence of the stratification seen in the fjord which greatly reduces the vertical mixing within of the fluid.

As discussed, the data from Haugsværfjorden features similar characteristics as the data from Masfjorden. The plots in figure 4.3 clearly shows that Haugsværfjorden is stratified and is covered by a brackish surface layer. Above around 50 m the water is well ventilated and decreases in salinity as the surface is approached. At around 50 m a pycnocline is observable, which separates the hypoxic basin water from the rest of the fjord. The hypoxia seen in Haugsværfjorden is the most significant difference seen in the vertical profiles of Masfjorden and Haugsværfjorden. In contrast to Haugsværfjorden, the dissolved oxygen concentration is greater than 4 mL/L at all depths in Masfjorden, indicating good ventilation of the basin water. Considering that the depth of the outer sill of Masfjorden is 68 m deep, it is reasonable to assume that Masfjorden experiences significantly more high density intrusions and thus renewal of basin water than Haugsværfjorden. The stagnation periods in Masfjorden can be expected to last significantly shorter than in Haugsværfjorden.

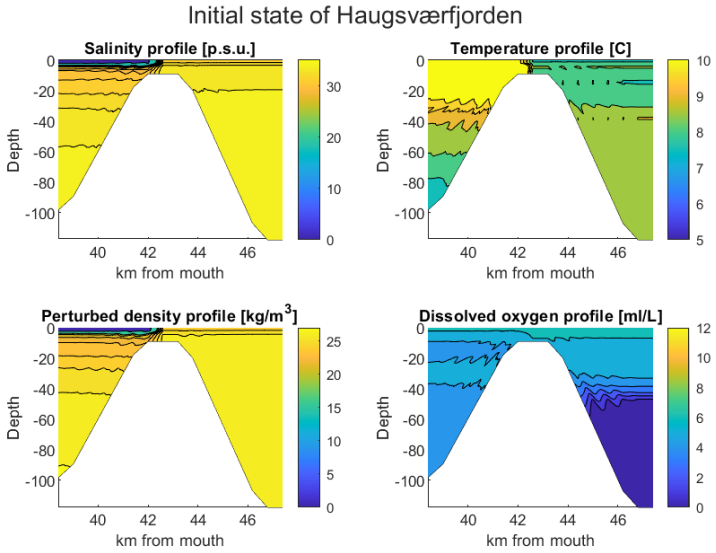

Figure 4.4: The state of Haugsværfjorden at the start of the simulation period. The figure shows the profile of the model immediately outside and inside Haugsværfjorden.

The initial state of Haugsærfjorden applied in the model can be viewed in figure 4.4. It is assumed that the vertical profiles in figure 4.2 and 4.3 are appropriate initial values for the entire system. Thus, the data from Haugsværfjorden initiates the fields inside Haugsværfjorden, while the data from Masfjorden initiates the fields in the rest of the model.

It can be observed in figure 4.4 that the salinity in the surface layer of Haugsvær-

fjorden and Masfjorden are different. This is most likely caused by seasonal variation or the large distance in time between the measurements. However, after an initial period of adjusting during the simulations, these differences in the surface layer are expected to vanish eventually.

The initial values of Masfjorden and Haugsværfjorden exhibits a wavy pattern near the slopes of the bottom topography. These waves originate from the interpolation used to assign values in the model. The measurements from Masfjorden and Haugsværfjorden are made at each meter through the water column, but in the model, the vertical grid points are distributed according to the σ-coordinate system. Thus, each σ-layer does not necessarily have the same thickness. In order to initiate the fields i σ-coordinates, a linear interpolation has been applied to the initial data. Since the σ-coordinate system is a terrain following coordinate system, the wavy patterns seen in figure 4.4 arises from the interpolation.

4.3 Boundary Conditions

As previously stated, there is a pool of water located between the mouth of Masfjorden and the outer sill which is represented in the model. In the model the depth of this pool is 150 metres in all cells. The western boundary of this pool is the only part of the model with non-constant boundary conditions. At this boundary the data from Sognesjøen is applied to the three westernmost cells in Masfjorden. In addition to this there is a relaxation method that applies a weighted sum of the data from Sognesjøen and the values of the fields in the pool outside Masfjorden in order to avoid computational noise.

The data from Sognesjøen has, as already mentioned, a frequency of around 14 days and the measurements available were made from 1, 10, 50, 75, 100, 150 and 200 m depth. In order to achieve a continuous change in the boundary conditions in the periods between the measurements at Sognesjøen, a linearly interpolated set of data is applied at the boundary. This data is both interpolated in time and space.

The data from Sognesjøen applied to the western part of the model is the primary driving force in the model. The fluctuations in the temperature, salinity and perturbed density at the boundary sets water masses in motion thus affecting the entire fjord system. The data from Sognesjøen does not include measurements of the dissolved oxygen concentration. Therefore the dissolved oxygen concentration of water entering the model domain is set constant in time. The vertical profile of the constant dissolved oxygen concentration in the entering water masses can be seen in figure 4.5.

The boundary conditions are constant everywhere in the model except at the western boundary where the dynamic boundary conditions discussed above is applied. In the model, there are two rivers, one in Matresfjorden and one in Haugsværfjorden. These rivers are represented at the two easternmost cells in which there is a constant flux of fresh water entering the model. Letting all the fresh water enter the fjord in a single location is a simplification since in reality

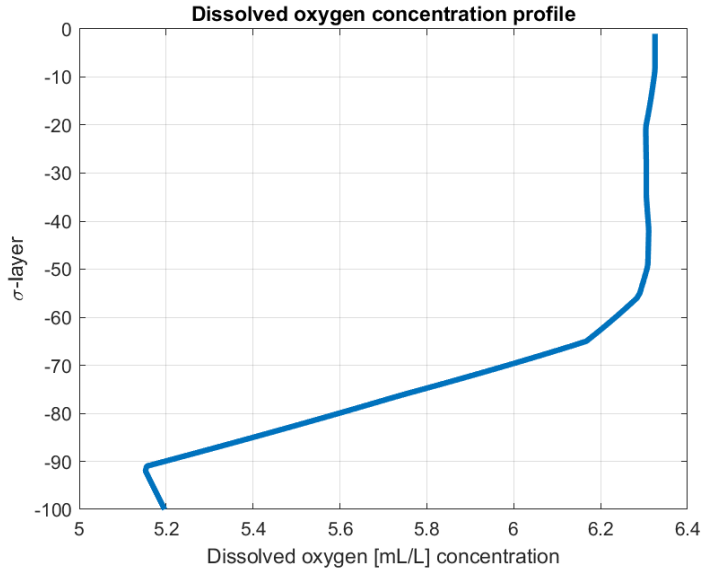

Figure 4.5: The dissolved oxygen profile of the water entering the model domain. The 100 σ-layers in the plot are distributed over the 150 m depth outside Masfjorden.

fresh water enters the fjords at many points, albeit most of it in the fjord heads, but this simplification is not regarded as overly unrealistic.

The fresh water enters the model in the upper 20 σ-layers at the eastern cells of Haugsværfjorden and Matresfjorden. In Haugsværfjorden this corresponds to letting the fresh water into the fjord in the upper 6 m. Additionally, a relaxation method is used such that the fresh water release is largest near the surface. The discharging fresh water has the constant salinity, temperature and dissolved oxygen concentration at 0 p.s.u., 6 C and 14 mL/L, respectively. Depending on the scenario, either both rivers has a flux of 0 m^3/s or the river in Matresfjorden has a flux of 155 m^3/s while the river in Haugsværfjorden has a flux of 10 m^3/s.

In the third scenario a submerged fresh water source is introduced at the sill floor. This means in practice that there is a constant flux of fresh water entering the fjord through the basin floor. In Haugsværfjorden this source is situated at 120 m depth, and during the simulation described later, the flux of the submerged discharge is constantly at 0.5 m^3/s.

In the previous chapters, the model and the domain it is mimicking has been described in detail. The following chapters will describe the three scenarios studied in this thesis.

Chapter 5

Scenario 1: The realistic case

With the above mentioned conditions the model was run for a 10 year simulation period from 2012 to 2022. The vertical profile of the four field variables salinity, temperature, density and dissolved oxygen concentration in the basin of Haugsværfjorden was stored for every 12 hours in the simulated period. The values of the mentioned fields below 50 m depth in the basin of Haugsværfjorden is plotted to a time series which can be seen in figure 5.1

The time series in figure 5.1 reveals an overall steady trend of dilution of the basin water of Haugsværfjorden. The salinity of the basin water generally decreases during the whole period, which can be seen in the upper left panel of figure 5.1. The difference in salinity between each isoline, or isohaline, in the first panel is 1 p.s.u.. The most saline water seen in the basin of Haugsværfjorden has a salinity of greater than 34 p.s.u.. At the end of the the simulated period, the deepest water has a salinity of around 32 p.s.u..

The temperature in the basin water generally decreases. However, the temperature change in the basin is in fact very small, and in this scenario the temperature change is in general negligible. The temperature field in the basin can be seen in the upper right panel in figure 5.1 where the temperature difference between each isothermal is 0.1 C.

In the lower left panel it can be seen that the density of the basin water also generally decreases. The density is calculated according to equation 2.1.0.10, and depends on both the temperature and the salinity, but also on the square of the temperature and the product of the salinity and the temperature. According to equation 2.1.0.10, the decrease in density is consistent with an increasing salinity but inconsistent with a decreasing temperature. However, since the temperature change in in the basin is very small the decreasing temperature has a negligible effect on the density of the basin water. At the start of the simualtion, the density of the water at the basin floor, ρ_b, has a measured

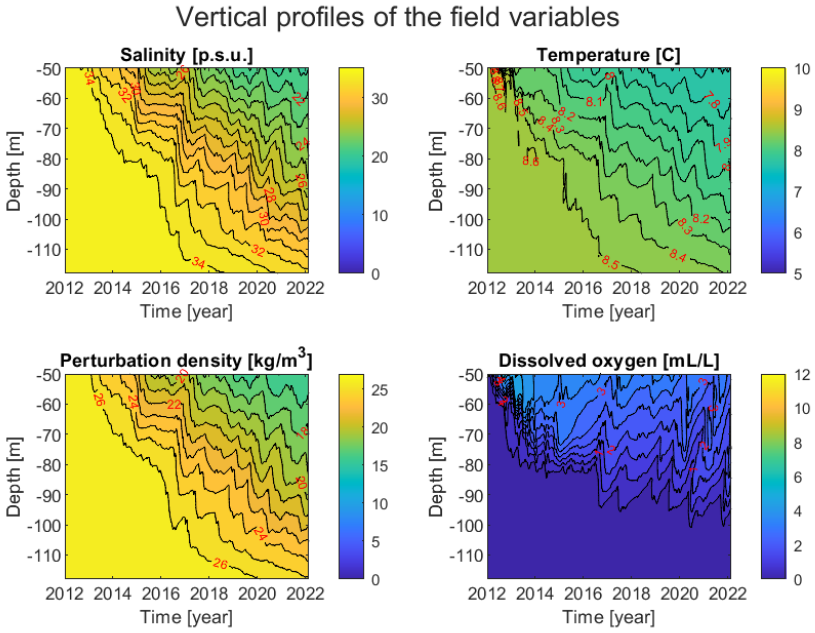

Figure 5.1: The evolution of the field variables below 50 m depth in the basin of Haugsværfjorden.

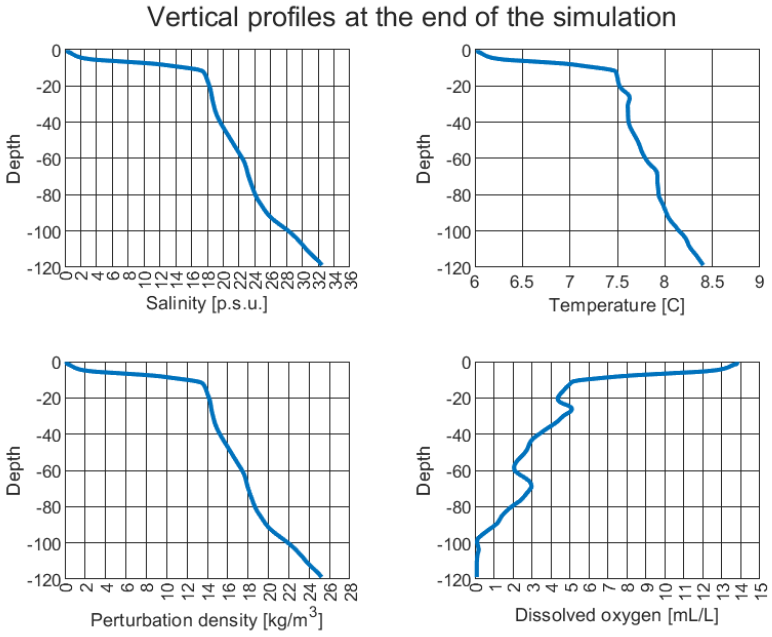

Figure 5.2: The vertical profiles of the salinity, temperature, perturbed density and dissolved oxygen concentration in the basin of Haugsværfjorden at the end of the simulation.

density of $\rho_b \approx 1026.99$ kg/m^3, and at the end of the simulation $\rho_b \approx 1025$ kg/m^3. The density difference between the isopycnals in the third panel is 1 kg/m^3.

In the lower right panel, the dissolved oxygen concentration of the basin water is displayed. In this plot the difference between isolines is 0.5 mL/L. Below around 100 m of depth the dissolved oxygen concentration is less than 0.5 mL/L during the whole simulation period. At the start of the simulation the 0.5 mL/L isoline is found higher up in the basin water at around 50 m depth, which means that the basin has been somewhat ventilated during the simulation period. However, the 2 mL/L isoline fluctuates at around 70 m depth for most of the simulation. Thus, the water below around 70 m is still hypoxic after 10 years, which is a severe restriction for life in the ocean Stigebrandt and Aure (1989).

In figure 5.1 it can be observed that the field variables steadily changes values with increasing depth at the end of the simulation. The vertical profiles of the four field variables at the end of the simulation is shown in figure 5.2

In all panels of figure 5.2 a significant difference in the surface water and the basin water is observable. The surface layer is characterized by a strong pycnocline and halocline producing the stratification in the fjord which is seen in the two left panels of figure 5.2. A large negative density gradient, $\partial\rho/\partial z$, which is observed in the pycnocline, greatly restricts the turbulent mixing in the model as described by the equations in subsection 2.2. However, it is in the surface layer the greatest velocities are expected in the fluid. Thus, the mixing of the surface layer and basin layer depends on the balance between the stratification and the vertical velocity shear. The surface layer is rich in oxygen and has a very low salinity since it mainly consists of river discharge from the fjord head. The river discharge has a salinity of 0 p.s.u., a dissolved oxygen concentration of 14 mL/L and a temperature of 6 C, which is nearly identical with the surface layer. Thus, the river discharge mixes mainly with the surface layer and will in general cause the surface layer to flow westward. Immediately below the pycnocline the four field variables changes nearly linearly with increasing depth.

Comparing figure 5.2 to the initial values of Huagsværfjorden in figure 4.3 it is clear as the depth increases the water in the basin is more akin to the original basin water. However, initially it is not the case that the field variables changes linearly with increasing depth. In fact, a second pycnocline at slightly above 50 m that separates intermediate basin water and deep basin water was present at the start of the simulation. At this time, the water below 50 m depth was very homogeneous water of high salinity and very low dissolved oxygen concentrations. While the basin water is expected to be diluted during the simulation, the change in the vertical profile from the initial state to the state at the end of the simulation is likely caused by numerical diffusion in the model.

However, at the bottom of the basin, below 100 m, the water is still severely hypoxic at the end of the simulation period. The continuous hypoxia of the deepest water may suggest that there has been no significant high density intrusions bringing new water and oxygen to the basin floor. If such a high density intrusion is to occur, the density of the water at the bottom of the sill, ρ_s, must

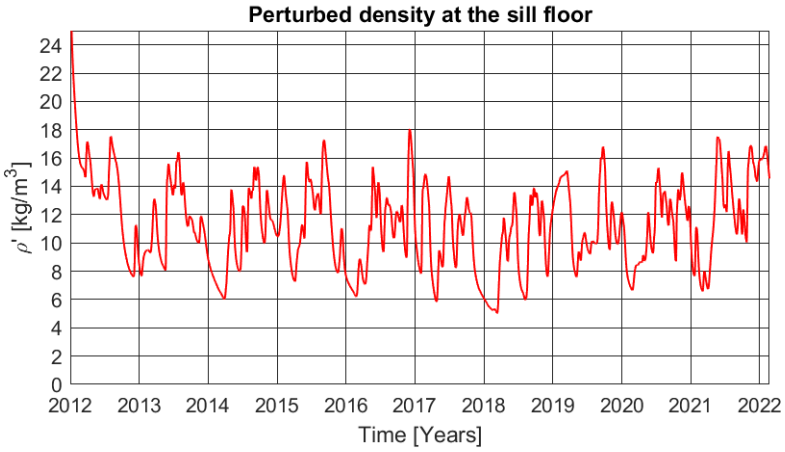

Figure 5.3: The evolution of the perturbed density at the deepest point of the sill, ρ_s. The local maximum value at the end of 2016 is $\rho_s \approx 1018.1$ kg/m^3.

exceed the density at the basin floor, ρ_b. In figure 5.3, ρ_s through the simulation period is presented.

In figure 5.3 it can be observed that ρ_s is initially significantly larger than during the rest of the simulated period. At the start of the simulation $\rho_s > 1024$ kg/m^3 while the average of ρ_s is $\bar{\rho_s} \approx 1011.32$ kg/m^3. Thus, it is reasonable to conclude that the initial state of over the sill was not in a state of equilibrium.

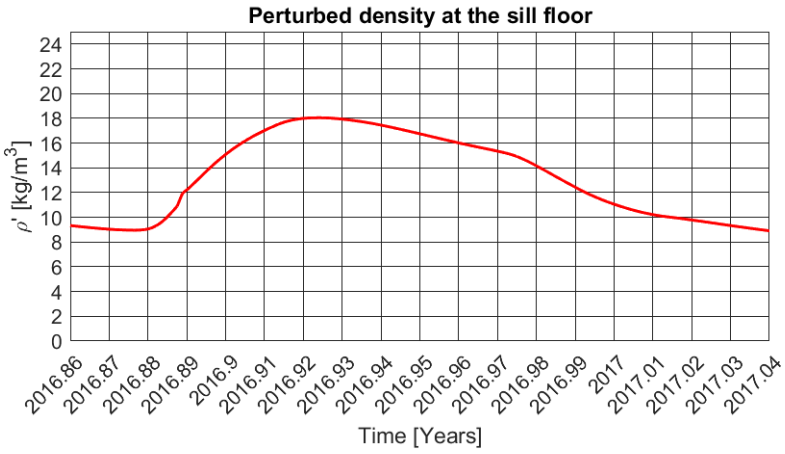

Figure 5.4: The figure shows the perturbed density of the water at the bottom of the sill during the intrusion event at the end of 2016.

However, $\rho_s < \rho_b$ throughout the entire simulated period. The minimum value of ρ_b is $\rho_b \approx 1025.2$ kg/m^3 while the maximum value of ρ_s is $\rho_s \approx 1018.1$ kg/m^3. Any period where $\rho_s > \rho_b$ must have lasted less than 12 hours, which is the frequency at which the output of the model was stored. But an event lasting shorter than 12 hours would most likely not bring a significant volume of dense

water into the fjord. In figure 5.4 the value of ρ_s around the time of the local maximum value of 1018.1 kg/m^3 is presented.

According to figure 5.4 $\rho_s > 1010$ kg/m^3 for around 0.14 years, which corresponds to 50.4 days (one year is 360 days in the model). Even though $\rho_s < \rho_b$ at least $\rho_s > \bar{\rho_s}$ for an extended period. In fact, $\rho \approx 1008.2$ kg/m^3 at around 10 m depth in the basin. Thus, the density gradient at 10 m depth, $\partial\rho/\partial x < 0$, will cause a flow into the basin along the sill floor. Judging by the longevity of the period when $\rho_s > \bar{\rho_s}$ any intrusion event lasting less than 12 hours seems unlikely to make a large impact on the fjord. However, the duration and intensity of the period with a relatively high ρ_s might suggest that an intrusion event occurred in the model around the end of 2016. In figure 5.5 the profile of Haugsværfjorden at this time can be seen.

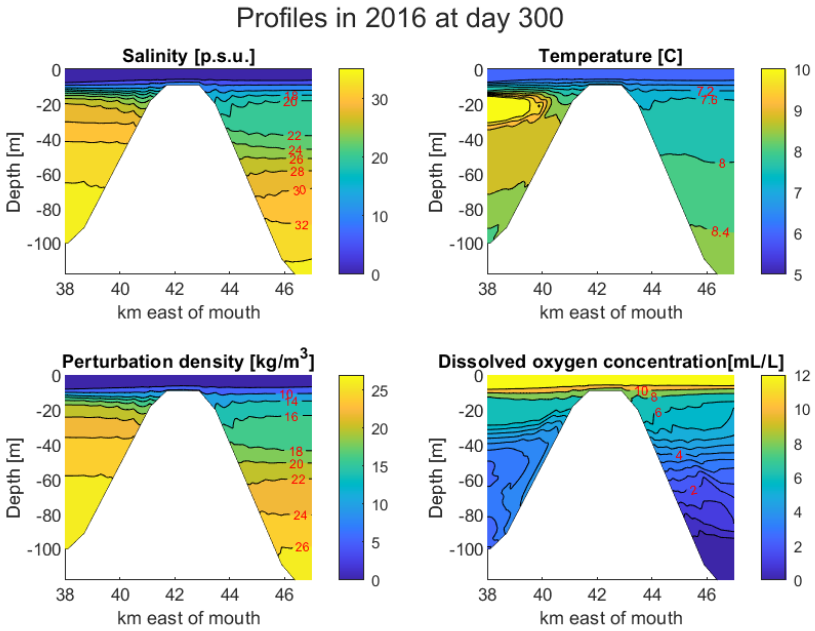

Figure 5.5: The profiles of the salinity, temperature, perturbed density and dissolved oxygen concentration fields in 2016 at day 300. This date converted to years corresponds approximately to the date 2016.83

The profiles of the salinity, temperature, perturbed density and dissolved oxygen concentration of Haugsværfjorden from figure 5.5 shows four rather undisturbed fields, but there are significant differences in the fields east and west of the sill. Generally the water east of the sill has lower salinity and dissolved oxygen concentrations than the water west of the sill at equal depths. The dissolved oxygen concentration field is somewhat dragged towards the sill along the fjord floor from the west. This might indicate a flow towards the sill at or before the instant in the figure, but it can also be evidence of an upwelling current along the fjord floor induced by the generally westward bound surface current. The isopycnal at 1010 kg/m^3 is approximately at the sill depth to the east of the

sill. Thus, the density in the basin at sill depth at the time seen in figure 5.5 is significantly smaller than the maximum value of ρ_s seen in figure 5.4 which occurs around 30 days later.

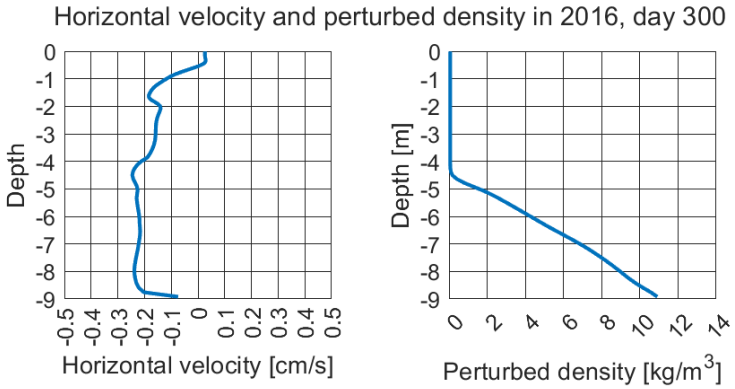

Figure 5.6: The horizontal velocity and ρ' over the sill in 2016 at day 300.

According to figure 5.6 the horizontal flow velocity at day 300 in 2016 is negative at all depths over the sill except in a thin layer near the surface that has a positive velocity. The eastward velocity of this thin upper layer is very small and can be neglected as this flow most likely terminates just east of the vertical profile due to the river discharge pushing westward at the surface. However, there is no evidence of a high density intrusion at day 300 in 2016. Figure 5.6 shows that $\rho_s > 1010$ kg/m^3 and that the density linearly decreases from the sill floor to around 4 m depth. Above 4 m depth the density is virtually 1000 kg/m^3 which means that this is practically fresh water. Since $\rho \approx 1010$ kg/m^3 at around sill depth in the basin, $\partial\rho/\partial x \approx 0$ at sill depth. Thus, the flow is largely controlled by $\partial\eta/\partial x$, seen in figure 5.10, which on average is positive east of the sill which explains why the water flows westward over the sill in figure 5.6. However, a slight increase in ρ_s will cause $\partial\rho/\partial x < 0$ at sill depth which will induce an eastward flow along the sill floor.

In figure 5.7 the fluxes over the sill between the dates 2016.86 and 2016.98 can be seen. The purple line is the flux of the bottom layer, Q_{in}, intruding eastward along the sill floor, while the yellow line is the flux of the surface layer, Q_{out}, leaving the fjord westward. It is clear from this figure that a high density intrusion event occurs in the time period in discussion. The orange line is the flux of a third layer, Q_3, which enters the fjord above the two previously described layers. Initially $Q_3 = 0$ m^3/s, but Q_3 increases as Q_{in} decreases near the end of the intrusion event. At the peak of the intrusion the flux of the dense intruding water is $Q_{\text{in}} \approx 11.8$ m^3/s and this local maximum value is close in time to the local maximum value of ρ_s. In figure 5.8 the vertical profiles of the horizontal velocity and density over the sill at the near the peak of the intrusion event can be seen.

At day 330 in 2016, Q_{in} was close to its local maximum value during the intrusion event. The horizontal velocity profile in figure 5.8 reveals a two-way flow over

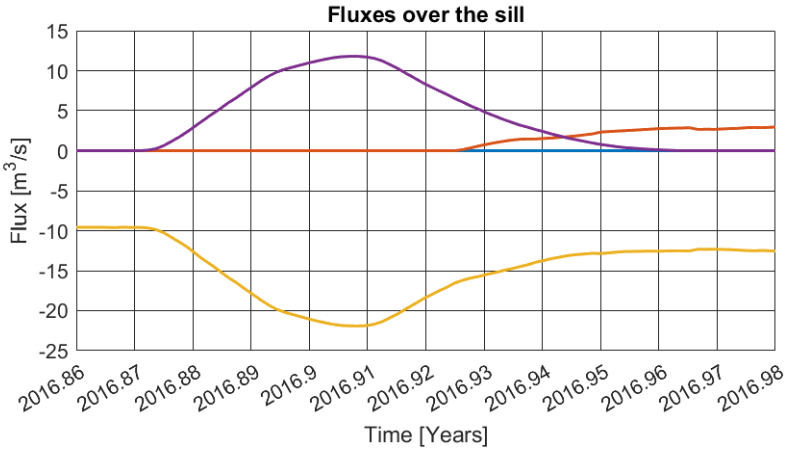

Figure 5.7: The fluxes over the sill between date 2016.86 and 2016.98.

the sill. Below around 6 m the water has a relatively high density and flows eastward along the sill floor into Haugsværfjorden. Above around 6 m the water has a lower density and flows westward out of Haugsværfjorden. The density of the surface layer has increased in comparison to the values seen 30 days earlier in figure 5.6. The most dense water leaving the fjord has a density of $\rho \approx 1010$ kg/m^3 which was approximately the density ρ_s at the sill floor 30 days earlier. The fact that density of the surface layer has increased indicates that there must have been a displacement of some volume in the basin.

In figure 5.9 the circulation during a high density intrusion event can be observed. Immediately above the sill floor, intruding water masses flowing eastward can be seen. The bottom layer over the sill has a smaller thickness at the eastern end of the sill than at the western end. The flux of a fluid layer is inversely proportional to the area it passes through, thus the decreasing thickness of the layer produces increasing velocities as the intruding flow moves eastward, which can clearly be observed in figure 5.9. Due to the river discharge there is a continuous flux out of Haugsværfjorden, but the increasing flux into the fjord demands an equally large flux out of the fjord. The water masses that are replaced by the intrusion is forced upwards which in turn increases the flux of the westward surface current. In figure 5.9 it can be seen that the westward current has a larger velocity at around 5 m depth than at the surface at the western side of the sill. The fact the upper part of the surface layer slows down above the sill might be due to an increasing thickness of the layer, but this slowing might produce downwelling over the sill. However, the magnitude of U is not very large but definitely larger than the magnitude of W by orders of magnitude. Thus, the effects of downwelling over the sill is most likely negligible.

The slowing of the surface flow seen in figure 5.9 can be explained by observing η in figure 5.10. On average, the surface elevation, η, attains a local minimum value over the sill of Haugsværfjorden. $\partial\eta/\partial x$ produces a flow in the opposite direction of the gradient, and judging only by the average of $\partial\eta/\partial x$ there will be converging currents at the surface over the sill. This convergence might

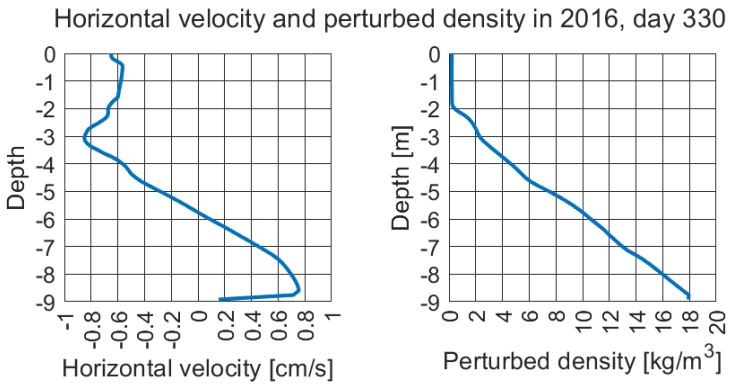

Figure 5.8: The vertical profile of the horizontal velocity and perturbed density over the sill at day 330 in 2016, which is near the time of largest eastward flux during the intrusion event.

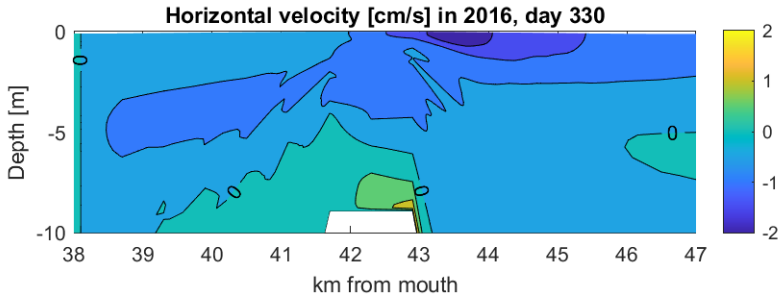

Figure 5.9: The horizontal velocities at day 330 in 2016 above 10 m depth are presented. A positive value corresponds to an eastward flow, while a negative value corresponds to a westward flow.

very well occur, and most likely does so at the end of the intrusion event when $Q_3 > 0$ m^3/s which can be seen in figure 5.7. The fact that $\partial\eta/\partial x < 0$ on average when x is in the range of approximately 39 to 43 km east of the mouth of Masfjorden is most likely due to the river discharge at the head of Matresfjorden. The fresh water discharging in Matresfjorden enters Masfjorden and will eventually enter Haugsværfjorden. At some point the currents from the two river discharges are balanced which creates convergent currents. The exact location of the convergence depends on the magnitudes of the different fluxes into Masfjorden and Haugsværfjorden and is most likely highly variable since these variations ultimately are caused by fluctuations in the boundary conditions.

According to figure 5.7 the intrusion event started around year 2016.87 and was ended around year 2016.96. Thus, the intrusion lasted around 32 days, whixh is not as long as the approximately 50 days when $\rho_s > 1010$ kg/m^3. During these 32 days a total volume of approximately $15.8 \cdot 10^6$ m^3 of water entered Haugsværfjorden. The volume of the intrusion is around 8,9 % of the total

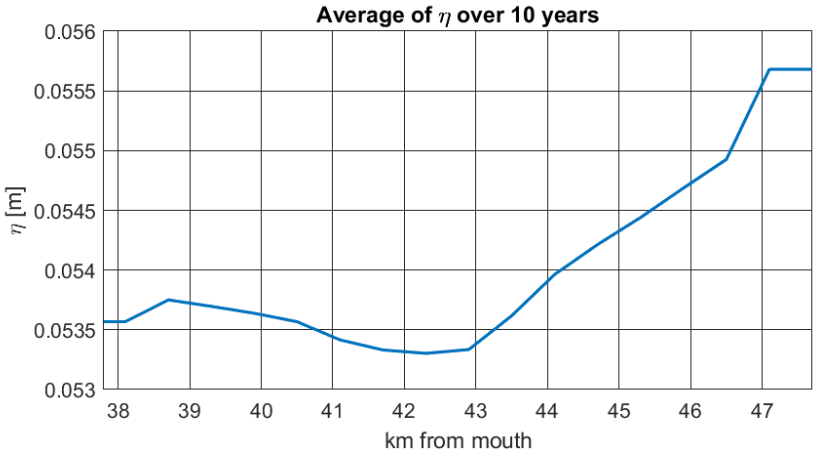

Figure 5.10: The average surface elevation, η.

basin volume in the model, which is approximately $177 \cdot 10^6$ m^3. However, the density of the intruding water was at most 1018.1 kg/m^3, which means that the intruding water could not have caused renewal of deep basin water. This is clear from figure 5.11

In figure 5.11 the differences in the salinity and density fields east and west of the sill are seen to be significant. At the instant depicted in figure 5.11, the flux of the intruding water, Q_{in}, is around its peak. The water west of the sill is significantly more dense than the water in Haugsværfjorden east of the sill. At the sill floor $\rho_s \approx 1018$ kg/m^3, a density which is found at around 40 m depth in the basin, which is a significant difference and a driving force of the intrusion. In both the salinity and density fields some of the isolines increase in height as the sill is approached from the east, which is especially apparent in the isopycnals at 1016 kg/m^3 and 1017 kg/m^3. Due to the fact that the intruding water shares properties with the intermediate water in the basin it is reasonable to believe that the volume of water in the intermediate layers of the basin water has increased. In figure 5.11 it is apparent that the increase in volume is concentrated to the west of the basin, which is explained by the fact that the dense intruding water flows along the floor of the fjord until the buoyancy of the water is neutral. Thus, the intruding water sinks until the surrounding water is at the same density. In the temperature and dissolved oxygen concentration fields the vertical motion of the intruding water masses is more apparent. The isothermal at 8 C in the temperature field distinctively follows the fjord floor, indicating that the water at the sill and along the floor down to 50 m depth shares a similar temperature, indicating the relation between the water masses. In the dissolved oxygen concentration field, it is apparent that there is a vertical transport of oxygen from the surface and downward along the slope into the basin. The oxygen is transported vertically towards the basin inside the sinking water masses of the intrusion. The dissolved oxygen field also reveals that the intruding water mixes with the surrounding water while it moves along the fjord floor. When the dense water enters the basin there will be instants when $\partial\rho/\partial z > 0$ below the intruding water, which increases the turbulent mixing and

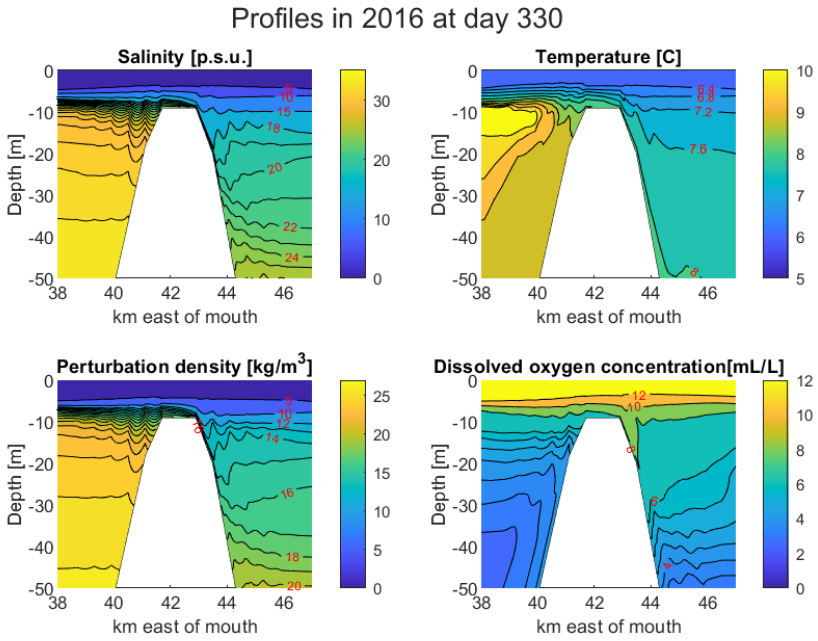

Figure 5.11: Profiles of the salinity, temperature, perturbed density and dissolved oxygen concentration at day 330 in 2016 above 50 m depth.

the mixing coefficients as described in subsection 2.2. When these sinking water masses mix with the surrounding water, the oxygen is mixed along with the water and there is a larger dissolved oxygen concentration along the fjord floor.

In figure 5.12 a more detailed view of the profiles over the sill is shown. From figure 5.12 it is clear that $\partial\rho/\partial x < 0$ at around 10 m depth, which induces an eastward flow at the sill floor. The isopycnals at 1016 kg/m^{3}and up to 1014 kg/m^3 follows over the eastern edge of the sill and along the fjord floor toward the basin. As described, the eastward bound water masses at the sill floor will start to sink when entering the basin of Haugsværfjorden due to negative buoyancy, which explains why there is a thin layer of dense water following the floor of the fjord eastward.

The pattern of isolines following the sill and fjord floor eastward is also seen in the salinity and temperature profiles in figure 5.12, and is explained by the same process. The dissolved oxygen concentration profile also shares similar features with the density profile. However, in the dissolved oxygen concentration profile the vertical transport into the basin is more apparent. It is clear that the intruding water masses induces a downwelling of water directly above the eastern edge of the sill. The downwelling here is most likely very small, but is seen to transport oxygen rich water to a larger depth.

During the high density intrusion event in late 2016 a significant amount of dense water entered the basin of Haugsværfjorden, but the intruding water

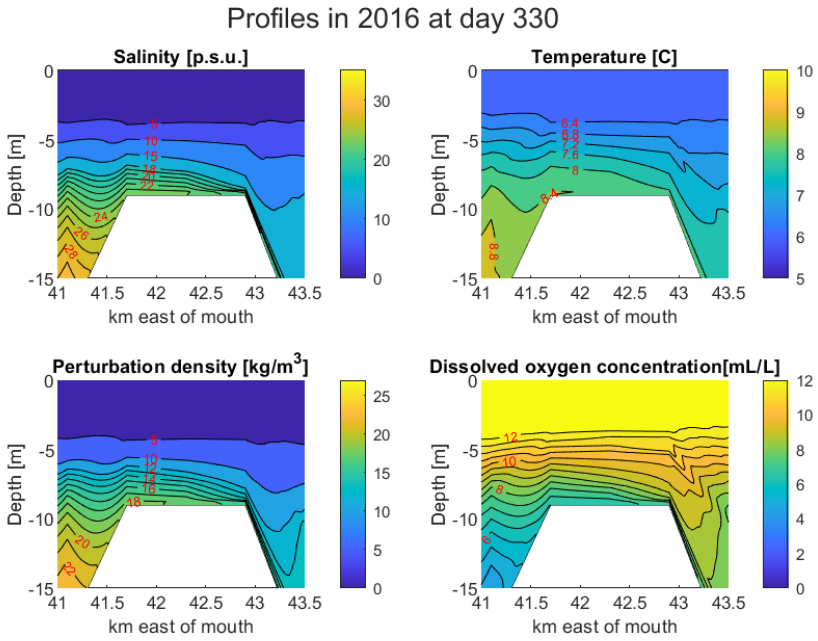

Figure 5.12: Profiles of the salinity, temperature, perturbed density and dissolved oxygen concentration at day 330 in 2016 above 15 metres depth.

masses did not sink to the basin floor. However, the intruding water masses did enter Haugsværfjorden and must thus have displaces some water elsewhere in the basin, renewing intermediate water in the basin.

In figure 5.13 there are signicifant spikes in the isolines at around late 2016. The isopycnal at 1018 kg/m^3 and 1020 kg/m^3 increase significantly around 2017. These spikes are not related to an increase in the volume of water at this density as $\rho_s < 1018$ kg/m^3 in general. The isopycnal at 1016 kg/m^3 steadily decreases during the intrusion period while the isopycnal at 1014 kg/m^3 is at a steady depth. This indicates that the volume of water in the range of 1014-1016 kg/m^3 has increased during the intrusion event. Thus, the intrusion may not have penetrated very deep into the basin, probably due to turbulent mixing of the intruding water causing it to rapidly decrease in density upon entering the basin. The rapid increases and decreases in the isolines below 40 m in figure 5.13 is thus possibly due to internal wavelike motions in the basin rather than intrusion events. After an intrusion event the density and other field variables at the depth where the intrusion renewed water masses is expected to rapidly change during the intrusion and then resume the steady pattern of stagnation after an intrusion. This pattern is only observed for the pycnocline at 1014 kg/m^3 in figure 5.13.

In the dissolved oxygen concentration field there are also spikes in the isolines at around the same depths as in the other profiles. This further establishes the fact that these spikes are not due to high density intrusions, since high density

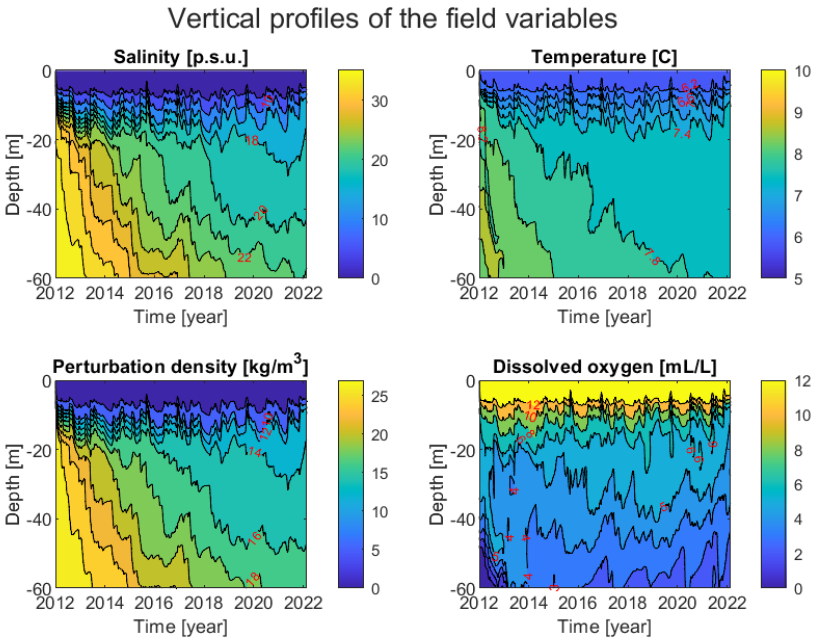

Figure 5.13: This figure shows the evolution of the field variables above 60 metres depth.

intrusions are expected to increase the dissolved oxygen concentrations which is the opposite of what is seen in figure 5.13. In addition to the effects of internal waves in the basin, the fact that the data presented in figure 5.13 is collected from the eastern part of Haugsværfjorden most likely reduces the visibility of high density intrusion events in figure 5.13. The intruding water masses may be so well mixed when reaching the eastern part of the basin that the impact on the density and other field variables is nearly negligible. Since ρ_s is not significantly larger than the basin water at around 20 m it is also quite likely that the intrusion overfills the intermediate layer it intrudes thus leading to the intrusion water itself being pushed out of the fjord in the circulatory pattern described earlier.

During the simulated period there are several intrusion events which can be observed when the density and fluxes over the sill is compared, as in figure 5.14.

The spikes in Q_{in} aligns nicely with the events where the ρ_s is higher than normal. The intrusion event that has received attention in this section is the one at the end of 2016. This high density intrusion is related to the maximum of ρ_s after the initial half year, and is one of few intrusion in which $Q_{\text{in}} > 10$ m^3/s. It should be noted that in figure 5.14 Q_{in} is the sum of all fluxes eastward over the sill, including low density intrusion at the surface. However, many of these intrusions will be high density intrusions since they coincide in time with large values of ρ_s. In figure 5.14 it can be observed that $|Q_{\text{out}}| > |Q_{\text{in}}|$ at all times. In fact, $|Q_{\text{out}}| \approx |Q_{\text{in}}| + 10$ m^3/s at all times. This is simply due to

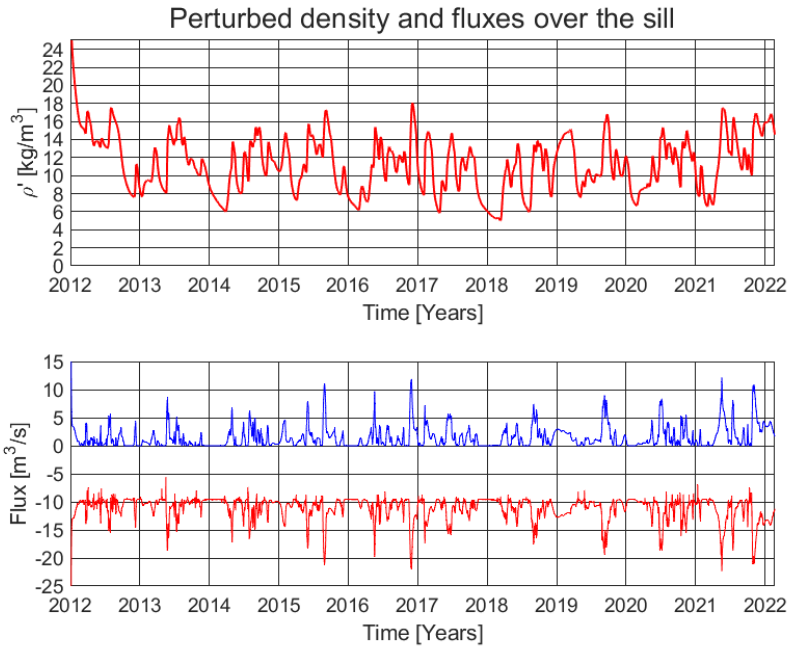

Figure 5.14: The density at the sill floor and the total fluxes over the sill compared. The blue line shows the eastward flux, Q_{in}, while the red line shows the westward flux, Q_{out}.

the constant river discharge from the head of Haugsværfjorden, thus asserting a constant net flux over the sill of $Q_{\text{net}} \approx -10$ m^3/s. Q_{net} is said to be constant, and is nearly just that. However, there will be some minor fluctuations in Q_{net} due to delays in the circulation upon increasing Q_{in}.

Using only ρ_s it is not possible to predict whether an intrusion event will occur or predict the intensity and duration of an intrusion event. The monitoring of the density at the sill floor relative to the density in the basin is a better tool to understanding the intrusions and their intensity and duration.

In figure 5.15 the evolution of the ratio between the density at the sill floor, ρ_s, and the density at the basin floor, ρ_b, throughout the simulated period is shown. The local maximum values in figure 5.15 matches the pattern of Q_{in} in figure 5.14 nicely. Figure 5.15 is very similar to the plot of the density at the sill floor from figure 5.14, but this figure reveals the potential of the intrusion. At most, the density at the sill floor is slightly above 99% of the density at the basin floor, which occurred a few times. These events are related to the most intense intrusion events. However, it never occured that ρ_s was more than 100 % of ρ_b. Thus, none of the intrusions into Haugsværfjorden has mixed with the deepest basin water, which explains why the water below 80 m in Haugsværfjorden remained stagnant during the entire simulated period. In order for an intrusion to sink to the basin floor a necessary condition on the ratio in figure 5.15 must at least be that

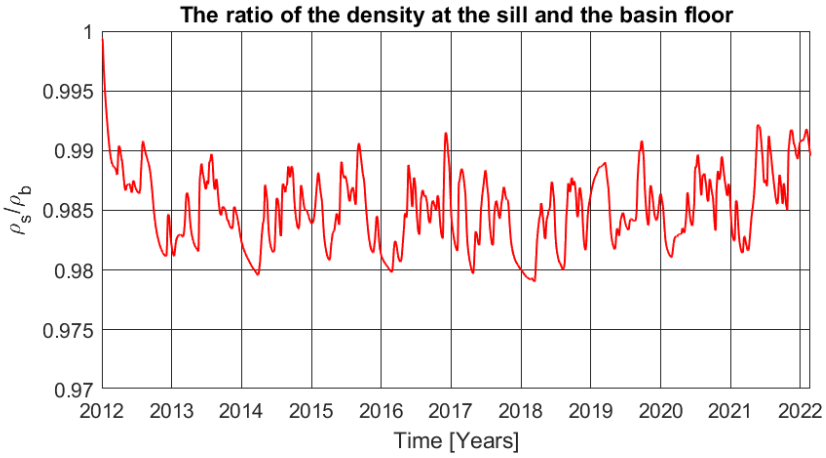

Figure 5.15: The ratio ρ_s/ρ_b through the simulated period is presented.

$$\frac{\rho_s}{\rho_b} > 1 \tag{5.0.0.1}$$

Thus, one of the necessary conditions needed for a high density intrusion into the basin of Haugsværfjorden is never fulfilled during the 10 year period. However, given enough time, the basin water is expected to be diluted sufficiently in order for $\rho_s/\rho_b > 1$.

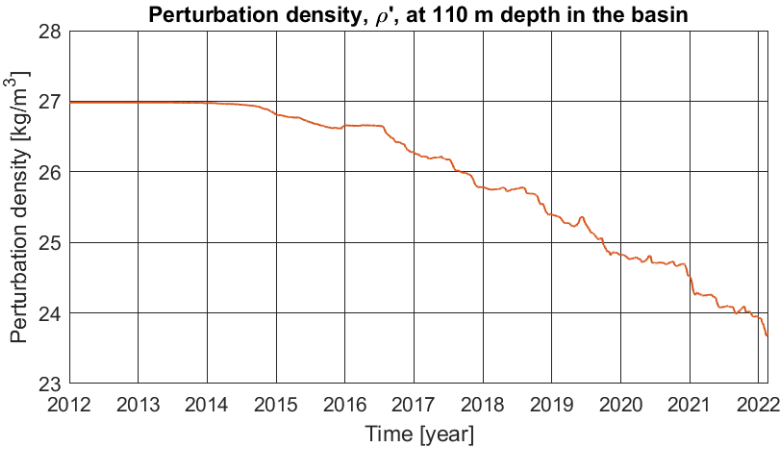

Figure 5.16: Initially $\rho_1' \approx 26.98$ kg/m^3, and at the start of 2022 $\rho_2' \approx 23.93$ kg/m^3.

The perturbed density, ρ', at 110 m depth, shown in figure 5.16, can be used to determine the average rate of dilution in the basin water. The most conservative approximation is yielded using the end points mentioned in figure 5.16

$$\frac{\partial \rho}{\partial t} \approx -0.305 \quad \text{kgm}^{-3}\text{yr}^{-1} \tag{5.0.0.2}$$

Thus, the density of the basin water in Haugsværfjorden approximately changes by -0.305 kg/m^3 per year. At this rate the density of the basin water $\rho_b \approx \bar{\rho_s} \approx 11.32$ kg/m^3 after just more than 41 years from the end of the simulation. When $\rho_s/\rho_b \approx 1$ there will be a balance in the system between the intrusion events and stagnation periods. Thus, it takes around half a century from the start of the simulation before the system in the model is in a state of equilibrium. Assuming that the linear decrease in ρ' seen from 2017 to 2022 continues, the rate $\partial\rho/\partial t \approx -0.45$ kgm^{-3}yr^{-1}. Using this approximation it takes 28 years in order for $\rho_b \approx \bar{\rho_s}$. However, since ρ_s fluctuates significantly, large intrusion into the basin floor might be expected already when $\rho_b = 1017$ kg/m^3. Assuming that high density intrusions into the basin floor will occur when $\rho_b \leq 1017$ kg/m^3, frequent high density intrusions can be expected around 2037, which is 15 years after the simulation stopped.

Nevertheless, the fact that $\rho_s/\rho_b > 1$ during the whole 10 year period is a major limitation in the probability of a high density intrusion in the system. The ratio ρ_s/ρ_b along with the circulation in the fjord surface layer is greatly affected by the constant river runoff. Firstly, the river runoff mixes with the surface layer which severely lowers the salinity and thus the density of the surface layer and hence the density over the sill. Secondly, at constrictions in an estuary or a fjord, hydraulically controlled flow is a great restriction on the flow into the fjord (Farmer and Freeland (1983)). In the case of a hydraulically controlled flow over the sill there is, according to Farmer and Freeland (1983), an upper limit to the two-way transport capacity through a constriction in an estuary or fjord for a simple layered flow under steady conditions. This condition is expressed by Farmer and Freeland (1983) as

$$F_1^2 + \frac{\rho_1}{\rho_2} F_2^2 = 1 \tag{5.0.0.3}$$

Here $F_1 = \bar{U}_1/\sqrt{g'h_1}$ and $F_2 = \bar{U}_2/\sqrt{g'h_2}$ are nondimensional numbers similar to Froude numbers for the upper and lower layers respectively. $\bar{U}_1$ and $\bar{U}_2$ are the averaged flow speeds for the upper and lower layers, respectively, and h_1 and h_2 are the thickness of the respective layers. Similarly, ρ_1 and ρ_2 are the average densities of the two layers, and $g' = g(\rho_2 - \rho_1)/\rho_2$ is the reduced gravity.

For instance during the peak of the intrusion event in 2016 at day 330 seen in figure 5.8, the heights were $h_1 \approx 6$ m and $h_2 \approx 3$ m. An aggressive approximation yields $g' \approx 0.17$ m/s^2, $\bar{U}_1 \approx -0.01$ m/s and $\bar{U}_2 \approx 0.01$ m/s, which used in equation 5.0.0.3 results in

$$F_1^2 + \frac{\rho_1}{\rho_2} F_2^2 \approx 2.9 \cdot 10^{-4} \ll 1 \tag{5.0.0.4}$$

Both Froude numbers, $F_1 \approx 0.010$ and $F_2 \approx 0.014$, are considered very small due to the low flow speeds, thus the sum in the condition above is significantly

smaller than unity. The interpretation of this is that hydraulically controlled flow over the sill in this model is very unlikely. Thus, the flow of the upper layer does not restrict the flow of the lower layer significantly and vice versa. For a small Froude number, as in this case, the flow is called a subcritical flow. If the Froude number exceeds unity the flow is called critical and the restriction in equation 5.0.0.3 controls the transport over the sill. During this hypothetical scenario the inflow over the sill might completely stop due to the resistance in the fluid flowing out over the sill. In reality the flow speeds may be expected to be larger thus increasing the probability of hydraulically controlled flow over the sill, but this phenomenon is still highly unlikely in the modelled system.

Since the flow velocity of the westward moving surface layer is not significantly restricting the flow of the intruding water due to the low flow velocities, the fact that the surface layer is low in salinity might be one of the largest restrictions on the probability of a high density intrusion. The constant river discharges leads to the low salinity in the surface water of the fjord which in turn greatly reduces the density at the sill floor. It has been observed in this scenario that the density at the sill floor is not nearly great enough in order for a high density intrusion to occur. The depth of the sill floor is also a major factor restricting the ventilation of the basin, but the river discharges are causing the surface layer to have a low salinity and thus relatively low density even at 9 m depth.

Even though the deepest basin water was stagnant during the entire 10 year period, a certain amount of dilution was observed. The dilution in the basin water is mainly caused by the vertical mixing coefficients K_M and K_H. The flow velocities in the basin are negligible since there were no high density intrusions, which greatly restricts the turbulent mixing in the basin. However, the probability of a high density intrusion was in fact slightly higher at the end of the simulation than at the start, but there is required an additional 41 years of time before high density intrusions are estimated to occur frequently.

Chapter 6

Scenario 2: The ideal case

In the second scenario all conditions are the same as in the first scenario except for the fluxes of the rivers. In scenario 1 there are two rivers in the model with fluxes of 10 m^3/s and 155 m^3/s. In scenario 2 both rivers are set to 0 m^3/s. Thus, scenario 2 is an unrealistic situation, but the comparison to scenario 1 might be fruitful.

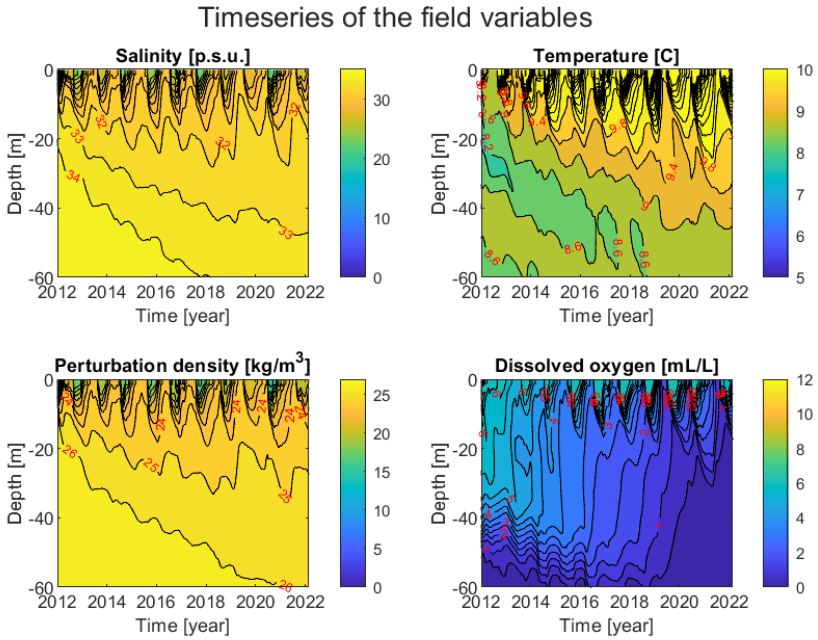

Figure 6.1: A timeseries of the model output for the variables salinity, temperature, perturbed density and dissolved oxygen concentration

In figure 6.1 the evolution of the salinity, temperature, perturbed density and

dissolved oxygen concentration above 60 m depth in Haugsværfjorden is presented. Similarly as in the first scenario, there is an overall trend of dilution of the basin water. However, the rate of the dilution is definitively smaller in the second scenario than in the first. This is not unexpected since the surface layer in scenario 2 has a much larger salinity than the surface layer in scenario 1. The turbulent mixing of salinity, heat and oxygen is proportional to the gradients in the respective fields. Even though the turbulent mixing is small, it will be the strongest force creating the dilution when the advection is negligible, which may very well be the case in the stagnant part of the basin water. The dilution is most clearly observed in the salinity field and hence the density field. In the density field, the pattern of dilution is seen in the isopycnal at 1026 kg/m^3. The same pattern can be seen in the isohaline at 33 p.s.u. and 34 p.s.u. At around 20 m depth and above, there are clear signs of intrusion events. Arguably, there occurred an intrusion event around the beginning of 2019 which also affected the salinity at around 40 m, which is observed in the isohaline at 33 p.s.u. Besides that, the pattern of the intrusion is featured in the isolines in all four panels of figure 6.1.

The same overall pattern is seen in the upper right panel of figure 6.1 which is presenting the temperature field. Below around 20 m, there is a steady dilution, while above 20 m there are several intrusions. The temperature field in scenario 1 was inverted due to the cold temperatures of the river discharge, but in the second scenario the temperature profile is not inverted, and the fluctuations in temperature are in fact much larger than in the first scenario.

In the lower right panel of figure 6.1, the profile of the dissolved oxygen concentration is presented. The pattern seen above around 50 m depth up to approximately 20 m depth is the pattern expected in stagnant water masses. In the model, oxygen is removed according to the equation

$$\frac{\partial O_2}{\partial t} = -b$$

where $b = 0.62$ mLL^{-1}yr^{-1} is the oxygen consumption per year. The oxygen consumption in the model is constant everywhere, but there is a constant minimum value of 0.1 mL/L. Assuming the intruding water masses have a relatively high dissolved oxygen concentration, the fact that the oxygen concentration steadily decreases during the simulation below around 20 m of depth is a strong indicator that intrusions does not in general sink deeper than around 20 m.

In figure 6.2 the vertical profiles of the salinity, temperature, perturbed density and dissolved oxygen concentration in the basin of Haugsværfjorden at the end of the simulation is presented. When figure 6.2 is compared to initial values of Haugsværfjorden in figure 4.3 it is clear that the basin water has been diluted.

In the initial state of the simulation the salinity was greater than 34 p.s.u. and the density was greater than 1026 kg/m^3 through most of the water column. Such levels of salinity and density are found only below around 60 m at the end of the simulation. The absence of a thick homogeneous basin layer at the end of the simulation is most likely caused by numerical diffusion. The

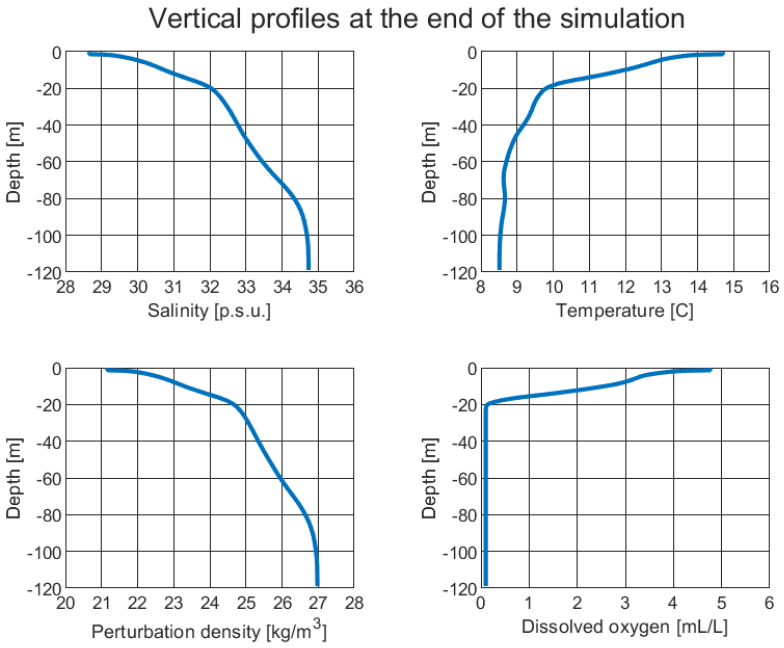

Figure 6.2: The vertical profile of the fiels variables at the end of the simulation.

temperature of the basin water below around 50 m has not changed significantly, but the temperature in the surface layer is significantly greater than in the initial state. This is clearly a result of the absence of the cold river discharge. Additionally there is no heat loss from the boundaries in the model, thus the only factor affecting the heat is the dynamic boundary conditions at the mouth of Masfjorden. The oxygen profile at the end of the simulation shows that the hypoxia in the basin water has become a lot more severe. Below 20 m depth the water is nearly anoxic. Such severe hypoxia was not observed above 50 m depth in the initial state in figure 4.3. The drastically low dissolved oxygen concentrations in the basin of Haugsværfjorden is most likely not only related to the absence of high density intrusions, but also related to the fact that there is no river discharge. Even though the constant flow of brackish surface water flowing out over the sill caused by the river discharge is a great restriction on the frequency of intrusions, the high oxygen concentration of the river water seems to have played an important role in the ventilation of the basin. Additionally, as previously stated, the intrusions in this scenario seems to primarily affect the water around 20 m depth and above, which is consistent with the hypoxia of the basin water below 20 m depth.

The high density intrusions seen in figure 6.1 seems to occur periodically. In fact there are exactly 10 significant high density intrusion events, thus the periodicity is most likely caused by seasonal variations represented through the dynamic boundary conditions. The seasonal fluctuations in the dynamic boundary conditions can be viewed in figure 6.3. During each year there is a period of low surface temperature coinciding with a high surface salinity, and oppositely

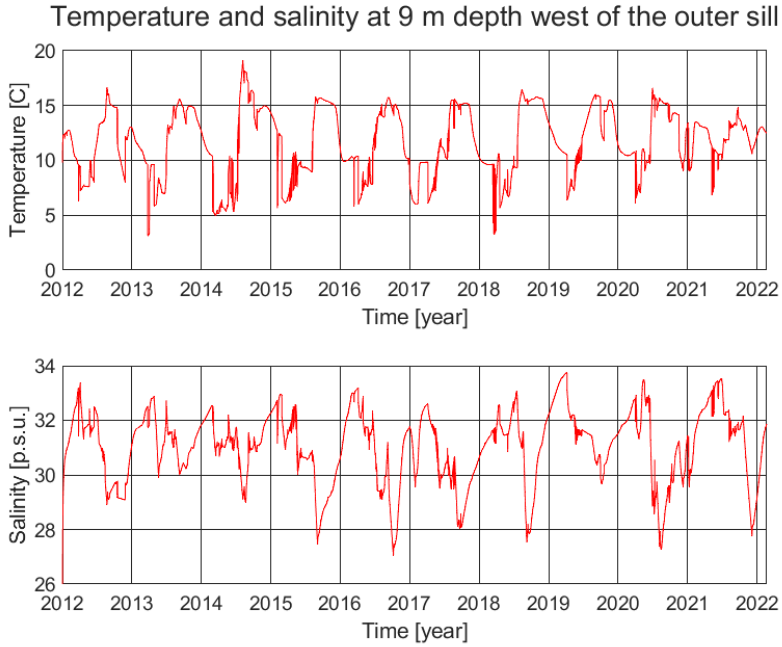

Figure 6.3: The temperature and salinity at 9 m depth west of the outer sill of Masfjorden.

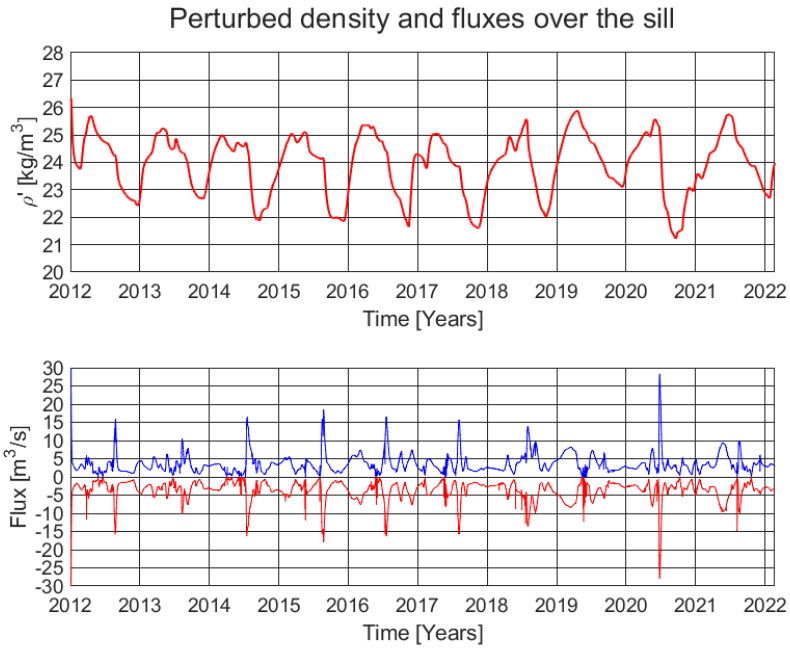

Figure 6.4: the perturbed density ρ_s' and the fluxes Q_{in} and Q_{out} during scenario 2.

a period of high surface temperature coinciding with a low surface salinity. The periods of high surface salinity can be recognized in figure 6.1 as the periods of the high density intrusions. The periods of low salinity, however, can be related to events of *low density intrusions*. The high density intrusions coincide with the periods of high salinity in the winter season during the first half of each year, while the low density intrusions occurs while the salinity is low in the summer season during the last half of each year. The fluctuations seen in the boundary conditions are caused by the seasonal variations in the surface temperature and salinity of the coastal water. In the winter, the probability of upwelling of deep oceanic water of high salinity and low temperature is more likely than during the summer leading to an annual period of high surface salinity. During the summer these events of upwelling along the coast are rarer than in the winter. Additionally, the snow at high eleveations above sea level in the south of Norway melts in the summertime leading to a large discharge of fresh water into the coastal surface water thus decreasing the surface salinity of coastal water.

From figure 6.4 it is clear that the seasonal variations in the density of the surface layer influences the probability of an intrusion into Haugsværfjorden. In figure 6.4 Q_{in} spikes at several points while some of the periods of a larger than normal Q_{in} over the sill has a longer duration and lower values. An example of each type of event is the largest spike in Q_{in} which is seen in 2020 and the long period of higher than normal value of Q_{in} seen in late 2018 to early 2019.

The intrusion related to the spike in Q_{in} in 2020 appears around halfway through the year and coincides with a sudden drop of ρ_s at the same time, which can be observed in figure 6.4. The fact that Q_{in} at this time occurs simultaneously with a low value of ρ_s suggests that this is in fact a low density intrusion event. Thus, this is an event where the water flowing into Haugsværfjorden has a lower density than the water inside the fjord, and the inflow of water is expected to occur at the surface of the fjord, starting a circulation which is the opposite of the circulation during a high density intrusion.

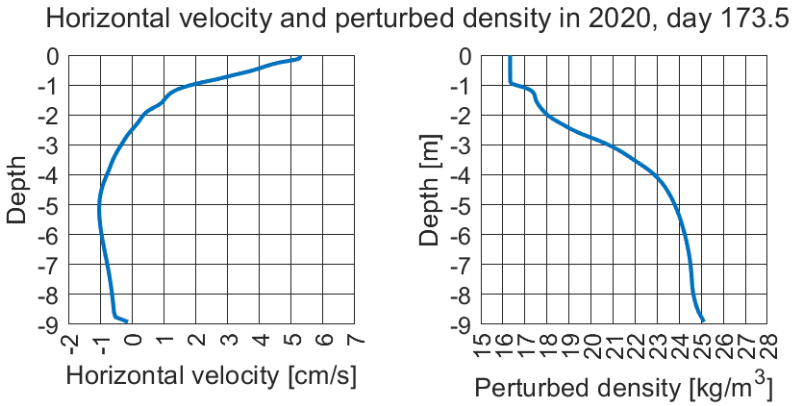

Figure 6.5: The horizontal velocity and ρ_s' during the peak of Q_{in} in 2020. At this time $Q_{\text{in}} \approx 28.4$ m^3/s.

From figure 6.5 it is clear that the intrusion event in discussion is in fact a low density intrusion. The upper layer over the sill is flowing eastward into Haugsværfjorden while the lower layer is a westward flowing countercurrent. The inflow into Haugsværfjorden has a lower density than the water leaving Haugsværfjorden over the sill. During this event there is a distinct two-way flow and the layers are separated at around 2.5 m depth. Using equation 5.0.0.3 to estimate the Froude numbers results in the still very low numbers $F_1 \approx 0.15$ and $F_2 \approx 0.02$. Thus, the flow over the sill is not close to being hydraulically controlled in this scenario as well.

Except for very close to the sill floor $\partial U/\partial z$ is quite small below 2 m depth, and the total change in flow velocity over these 7 m is less than 2 cm/s. Above 2 m depth $\partial U/\partial z$ is significantly greater than below this depth. The amount of turbulent mixing occurring in the instant depicted in figure 6.5 is related to the Richardson number for the flow. Using the Brunt-Väisälä frequency, $N = \sqrt{(-g/\rho)(\partial\rho/\partial z)}$, an estimate of the Richardson number in the upper 5 m during the event described above is

$$\mathrm{Ri} = \frac{N^2}{(\partial u/\partial z)^2} = -\frac{g}{\rho}\frac{\partial \rho}{\partial z}\left(\frac{\partial U}{\partial z}\right)^{-2} \approx 91.4 \gg \frac{1}{4} \qquad (6.0.0.1)$$

The Richardson number is significantly larger than the critical value 1/4, thus there is not nearly enough kinetic energy in the water to turbulently mix the two layers over the sill completely. An exception from this would be the in the upper meter of the surface layer over the sill. Here $\partial\rho/\partial z \approx 0$, which virtually yields a Richardson number $\mathrm{Ri} = 0$. According to the equations in subsection 2.2 the vertical velocity shear, $\partial U/\partial z$ will govern the turbulent mixing when $\partial\rho/\partial x = 0$.

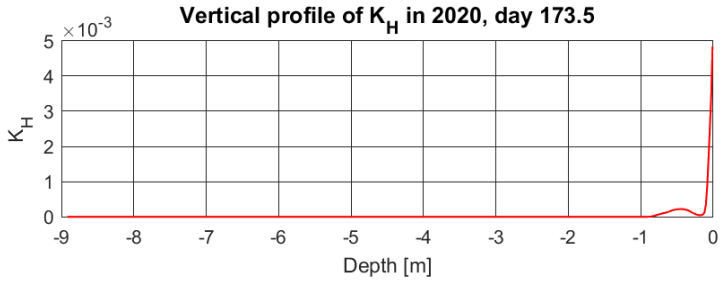

Figure 6.6: K_H in 2020, day 173.

The value of K_H is not very large, but the relative increase in K_H, seen in figure 6.6, near the surface indicates turbulent mixing at this depth. Both K_H and K_M grows proportionally to ql, thus an elevated value of K_H corresponds to an elevated value of K_M. The fact that $\partial\rho/\partial z \approx 0$ near the surface, in the instant depicted in figures 6.5 and 6.6, means that $\partial U/\partial z$ is large enough such that the turbulent mixing overcomes the stratification in the fluid. The fact that $\rho/\partial z \approx 0$ in the upper 1 m might be due to turbulent mixing, but can also be explained by the fact that the river water has not yet completely mixed into

the surface layer. In general, turbulent mixing seems unlikely in this scenario, and most likely Ri $> 1/4$ most of the time. If turbulent mixing occurs, it seems that it is most likely to happen during the periods when $|Q_{\text{in}}|$ or $|Q_{\text{out}}|$ are very large leading to large flow velocities.

As stated earlier, the periodic spikes in Q_{in} over the sill seen in figure 6.4 coincides with periods of low density. These annual spikes are related to an intrusion of water with low density at the surface of the fjord. During periods of higher density in the first half of each year, the spiking pattern is absent and a more steady increase and decrease of Q_{in} is observed. An example of this is the extended period of higher than normal Q_{in} at the start of 2019. This intrusion event has been discussed as an observation in figure 6.1. It is observed that the intermediate layer at $\rho \approx 1025$ kg/m^3 increases considerably in volume during the intrusion while the deeper layer at $\rho \approx 1026$ kg/m^3 is hardly affected by this intrusion.

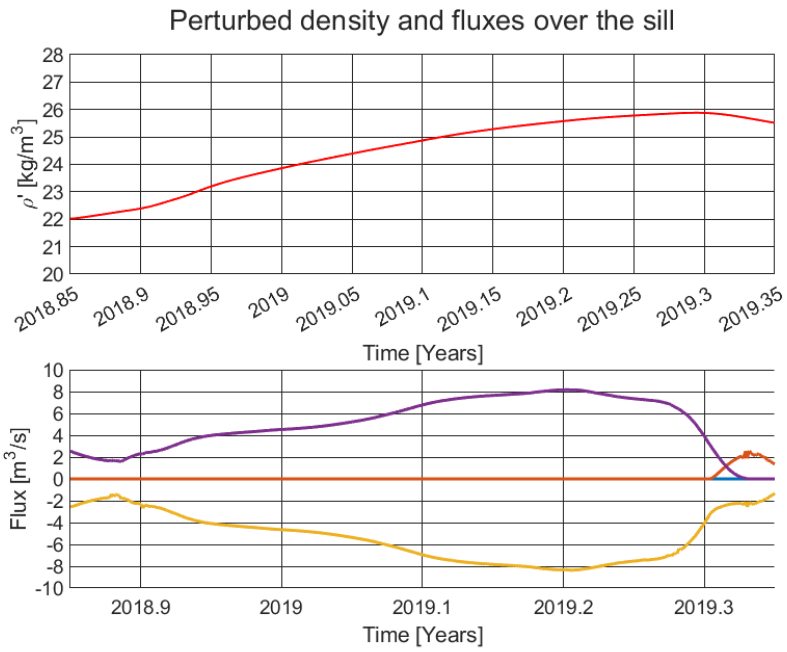

Figure 6.7: The horizontal velocity and the perturbed density at the peak of the intrusion in early 2019. The maximum eastward flux in this plot around 8.2 m^3/s.

The intrusion event in discussion starts at around 0.9 years or 324 days into 2018. At the same time ρ_s starts increasing, and it increases steadily until the maximum value of $\rho_s \approx 1026$ kg/m^3 around 0.3 years or 108 days into 2019. Q_{in} increasing simultaneously as ρ_s and reaches a maximum of around $Q_{\text{in}} \approx 8.2$ m^3/s at around the year 2019.2. Even though ρ_s is at a maximum at the date 2019.3, Q_{in} decreases rapidly at this date and a third flux, Q_3, increases around the same time. $Q_3 > 0$ is the flux of a third layer in the flow over the sill which is above both Q_{in} and Q_{out}.

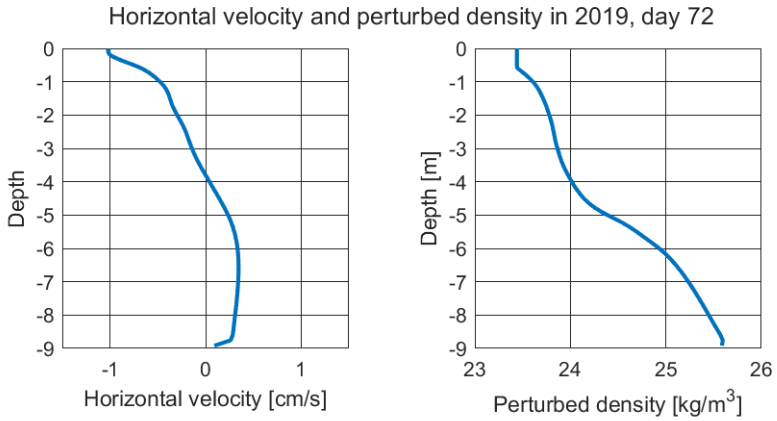

Figure 6.8: The velocity and perturbed density over the sill at the time of the maximum eastward flux.

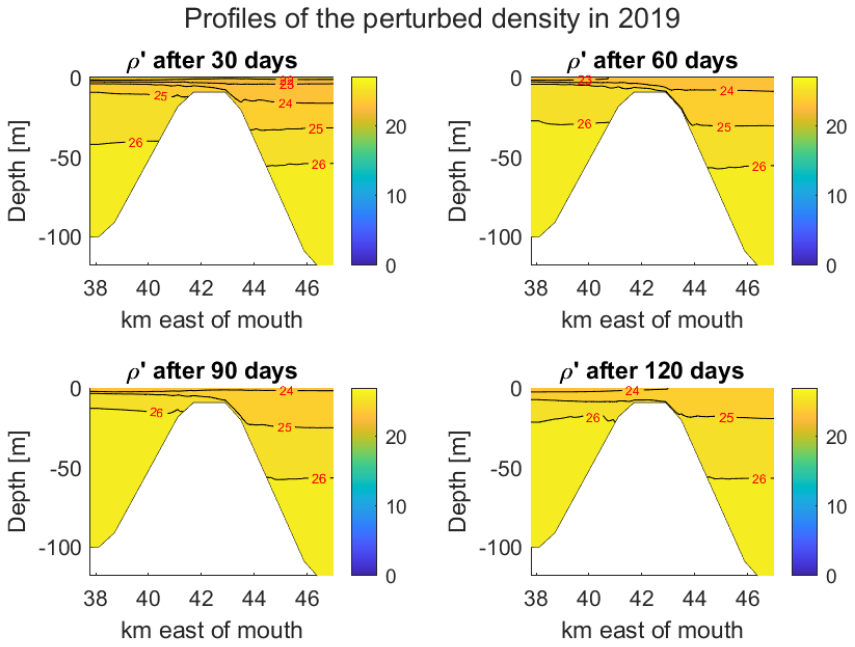

Figure 6.9: A selection of perturbed density profiles showing the volume increase in the intermediate layers during the intrusion event.

The vertical profiles of the horizontal velocity and the perturbed density over the sill at the peak of the intrusion is presented in figure 6.8. Clearly there is a two-layer flow over the sill, and the circulatory pattern during this event is exactly as expected during an high density intrusion event. Dense water enters the fjord along the sill floor, which causes a countercurrent at the surface. Since there is no river discharge in this scenario, $Q_{\text{in}} = Q_{\text{out}}$. The two layers are separated at around 4 m depth, where the upper layer flows westward while the lower layer flows eastward. Between 6 m and 4 m depth the magnitude of the vertical density gradient, $\partial\rho/\partial z$, is larger than elsewhere in the column seen in figure 6.8. Thus, there is a weak stratification over the sill inhibiting mixing of the two oppositely flowing layers as a strongly negative density gradient reduces the turbulence in the model. However, there is most likely some mixing between the two layers which may explain why the pycnocline is mostly within the lower layer rather than in both layers.

In figure 6.8 $\rho_s < 1025$ kg/m^3, which means that the intruding water masses can potentially sink to the depth in the basin at which $\rho_s = 1025$ kg/m^3 or deeper. As stated in section 5, the intruding water masses will mix with the surrounding water masses while sinking into the basin. However, the density of the intermediate water in the basin is only slightly greater than ρ_s, which means that the density of the mix of intruding water and the surrounding water will be quite close to ρ_s.

In figure 6.9 the evolution of the density field during the high density intrusion in discussion can be viewed. In the upper left panel of figure 6.9 the intruding water masses has a density of around $\rho_s \approx 1024$ kg/m^3. The isopycnal at $\rho = 1024$ kg/m^3 inside the sill is connected to this isopycnal outside the sill, which means that there is a continuous layer of density $\rho < 1024$ kg/m^3 throughout the fluid. The part of this layer that is immediately east of the sill has a negative buoyancy and sinks to around 20 m which is the depth of the pycnocline at $\rho = 1024$ kg/m^3.

In the upper right panel of figure 6.9 it can be observed that ρ_s has increased and that the thickness of the layer of density $\rho > 1024$ kg/m^3 has increased. Thus the volume of the intermediate water density between 1024 kg/m^3 and 1025 kg/m^3 in the basin has increased. This increase in volume has elevated the less dense water upwards and thus forced it to flow out of the fjord. These less dense water masses that are forced out of the fjord is what creates the countercurrent at the surface over the sill.

In the lower left panel of figure 6.9, it is seen that the volume of the intermediate layer of water of a density between 1025 kg/m^3 and 1026 kg/m^3 in the basin has increased. The less dense water in the surface layer, which is at a density of $\rho \approx 1024$ kg/m^3, is still being forced out over the sill. Thus, parts of the water that intruded the basin at the start of the intrusion event is flowing back out of the fjord. Outside the sill it can be observed that the isopycnal at 1026 kg/m^3 is elevated and is almost at the same depth as the sill floor. The rise of the 1026 kg/m^3 isopycnal is a response to an intrusion in Masfjorden caused by an increased density at the boundary. This specific intrusion into Masfjorden is related to the maximum density at the boundary observed in

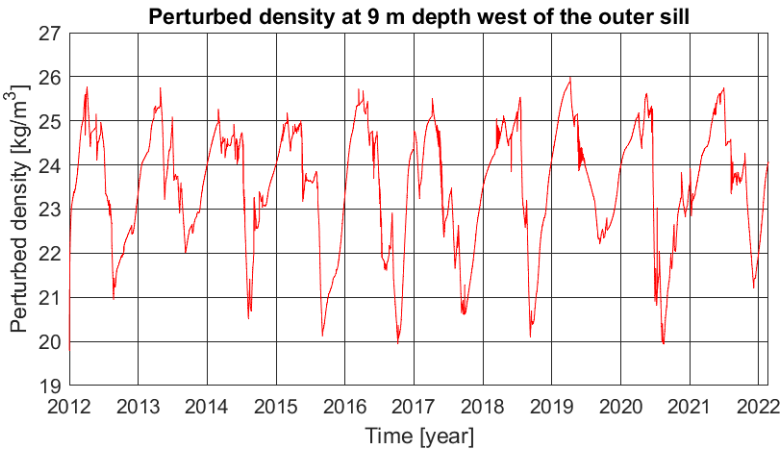

Figure 6.10: The perturbed density at 9 m depth outside the sill of Masfjorden. The maximum density is $\rho \approx 1026.04$ kg/m^3 and occurs 95 days into 2019.

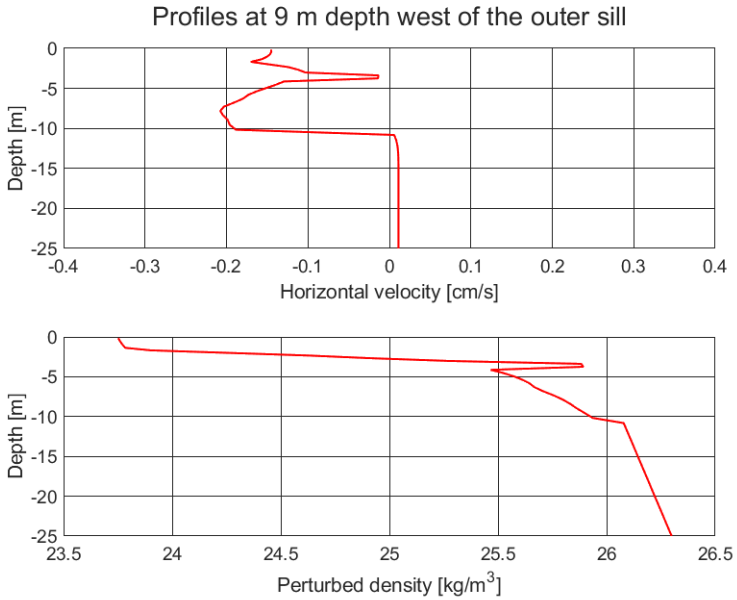

Figure 6.11: The horizontal velocity and the perturbed density west of the outer sill in 2019, day 95.

figure 6.10 at around 95 days into 2019 at which time the density outside the sill of Masfjorden at 9 m depth was $\rho \approx 1026.04$ kg/m^3. The vertical profile of the horizontal velocity and the perturbed density west of the outer sill of Masfjorden in 2019 at day 95 can be viewed in figure 6.11. The separation of the eastward flowing dense water and the westward flowing brackish surface layer is found at slightly below 10 m depth west of the outer sill. Since the flows are rather small around this depth the pycnocline seen just below 10 m depth likely inhibits any large amount of turbulent mixing between the two layers. However, the large density of the water below 10 m outside the sill of Masfjorden ensures that generally $\partial\rho/\partial x < 0$ below 10m throughout the fjord which induces a flow that fills Masfjorden with dense water which consequently pushes less dense water upwards and into Haugsværfjorden. The maximum density of the water flowing over the sill is in fact nearly 1026 kg/m^3 at around 108 days into 2019, which is nearly the same density as the water outside the outer sill at the same depth.

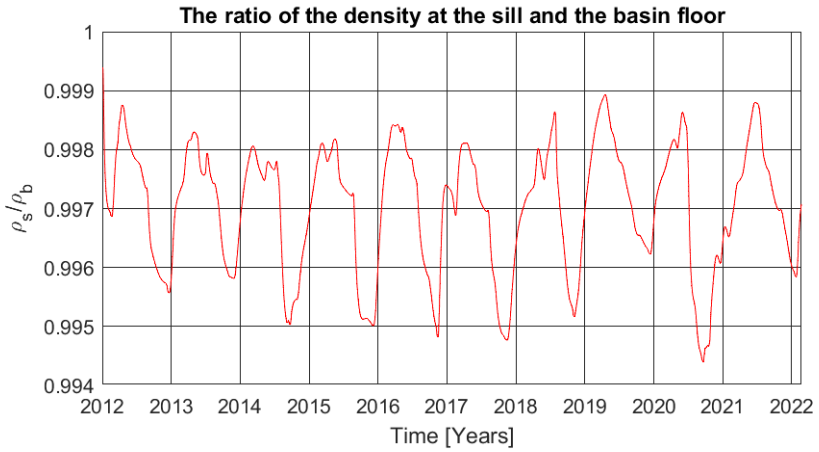

Figure 6.12: The ratio of the density at the sill floor and at the basin floor

In the lower right panel in figure 6.9, the volume of the intermediate layer of higher density than 1025 kg/m^3 is clearly larger than in the other panels. The isopycnal at 1026 kg/m^3 inside the basin is still at around the same depth, thus any masses of water that might have sunk below this isopycnal is negligible. In the lower right panel the isopycnal at 1024 kg/m^3 has nearly disappeared, and is very close to the surface. This means that the water of lower density than 1024 kg/m^3 is entirely pushed out of Haugsværfjorden. Thus, the countercurrant at the surface definitely includes some of the water masses that initially was a part of the intrusion leading to the suspicion that the intermediate layer is "over-filled", meaning that all the water above a certain depth has been replaced.

The total volume of the intrusion discussed here is approximately $75.5 \cdot 10^6$ m^3 which is around 42.7% of the basin volume. Since the maximum of $\rho_s < 1026$ kg/m^3 during the entire event no water intruded deeper than around 60 m, which is the depth at which the 1026 kg/m^3 isopycnal is situated. This isopycnal nearly divides the basin into an upper and a lower half. Thus, the intrusion that was at 42.7 % of the basin volume must have displaced nearly the entire upper half of

the basin. Additionally, since this intrusion coincided with the maximum of ρ_s during the 10 year period, there were likely no water of greater density entering the fjord at any other time during the simulation. Thus the basin water below around 60 m remained stagnant for the entire 10 year period.

In figure 6.12 the ratio between the density at the sill floor, ρ_s, and at the basin floor, ρ_b, is shown. When comparing this to the same ratio for scenario 1 which is seen in figure 5.15, it can be seen that ρ_s/ρ_b is generally much higher in scenario 2 than in scenario 1. In scenario 1 it is rare to see that $\rho_s/\rho_b > 0.99$, but in scenario 2 it is always true that $\rho_s/\rho_b > 0.99$. Thus it seems that the probability of a high density intrusion is more likely when there is no river discharge in the model. However, $\partial\rho/\partial t$ is likely significantly less in scenario 2 than in scenario 1.

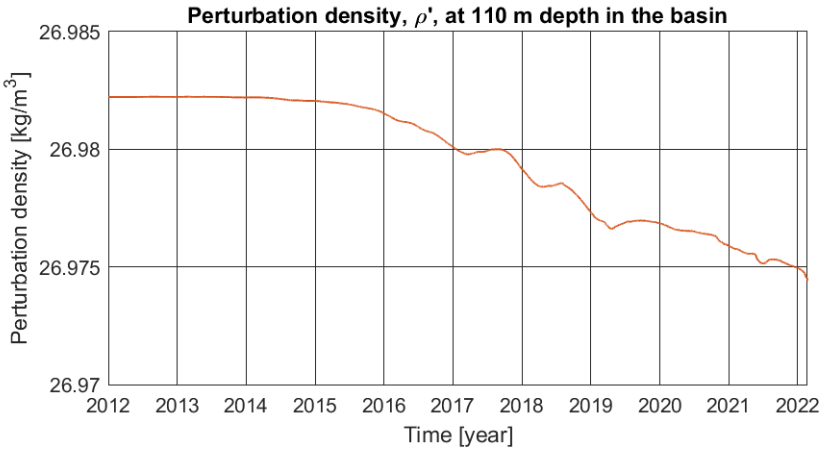

Figure 6.13: The evolution of ρ' at 110 m depth in the basin. Initially $\rho \approx 1026.9822$ kg/m^3 and at the start of 2022 $\rho \approx 1026.9750$ kg/m^3 at 110m depth in the basin.

In figure 6.13 the evolution of the perturbed density at 110 m depth in the basin is presented. Applying the values mentioned in figure 6.13, the approximation becomes

$$\frac{\partial\rho}{\partial t} \approx -7.4 \cdot 10^{-4} \quad \text{kgm}^{-3}\text{yr}^{-1} \tag{6.0.0.2}$$

At this rate $\rho_b \approx \bar{\rho_s} \approx 1023.93$ kg/m^3 after 4000 years. Assuming that the $\partial\rho/\partial t$ is the same as in the time between 2017 and 2022, the approximation becomes

$$\frac{\partial\rho}{\partial t} \approx -4.6 \cdot 10^{-2} \quad \text{kgm}^{-3}\text{yr}^{-1} \tag{6.0.0.3}$$

which means that $\rho_b \approx \bar{\rho_s}$ around year 2088. During the high density intrusion event discussed in scenario 2 it was observed that $\rho_s > 1025$ kg/m^3 for significant periods. Thus, assuming $\rho_s > 1025$ kg/m^3 is sufficient for a high density intrusion to sink to the basin floor, this can be expected around the

year 2060. The probability for a high density intrusion to sink to the basin floor is likely governed by ρ_s/ρ_b as well as the duration of the intrusion event. It is necessary that $\rho_s/\rho_b > 1$ and that the duration is long enough such that a significant amount of water intrudes the basin. Otherwise the intrusion is likely to completely mix into the intermediate basin water before reaching the basin floor.

However, during scenario 2 as in scenario 1, there were no intrusions into the basin floor and thus no renewal of the deep basin water. The high density intrusion discussed in scenario 2 had a significantly greater volume than the high density intrusion discussed in scenario 1. Thus, the conditions at the sill favored large intrusions more in scenario 2 than in scenario 1, which is most likely explained by the absence of the river discharge which controls the flow into the fjord. However, the stagnation periods are potentially shorter in scenario 1 as the magnitude of $\partial\rho/\partial t$ was significantly larger in scenario 1 than in scenario 2. Nevertheless, both the systems in scenario 1 and scenario 2 are prone to long stagnation periods in the short term.

Chapter 7

Scenario 3: Submerged fresh water discharge

In the third scenario all conditions are the same as in scenario 1, except that there is an artificial source of fresh water at the basin floor. Specifically there is a constant flux of fresh water at the boundary at the bottom of the basin in Haugsværfjorden in the model. The motivation behind a discharge of fresh water at the basin floor is to increase the magnitude of $\partial\rho/\partial t$ in the basin water which in turn decreases the duration of the stagnation periods. Additionally, the submerged fresh water source will induce some upwelling in the basin water, which might increase the ventilation.

According to Berntsen et al. (2022) the flux of the submerged source can be estimated using the equation

$$Q_F = \frac{\Delta\rho V}{T\left(\rho_A - \rho_0\right)} \tag{7.0.0.1}$$

here Q_F is the flux of the source, $\Delta\rho$ is the difference in density in the surface layer and in the basin, V is the basin volume, T is the time scale of the ventilation, ρ_A is the density of the water above the sill at the fjord entrance, and ρ_0 is the density of the water discharged from the submerged source.

In this scenario the estimate has been made using density data from Haugsværfjorden along with the volume of the fjord in the model. According to the data gathered in Haugsværfjorden in the years 2019-2021 $\Delta\rho \approx 2.27$ kg/m^3 and $\rho_A \approx 1024.4$ kg/m^3. The basin volume in the model is $V \approx 177 \cdot 10^6$ m^3, which is the volume of the fjord under the sill depth. The time scale is chosen at 1 year, so $T = 360 \cdot 24 \cdot 3600$ s, and the water discharging is fresh water with a density of $\rho_0 = 1000$ kg/m^3. Using these values, the estimated submerged fresh water flux is

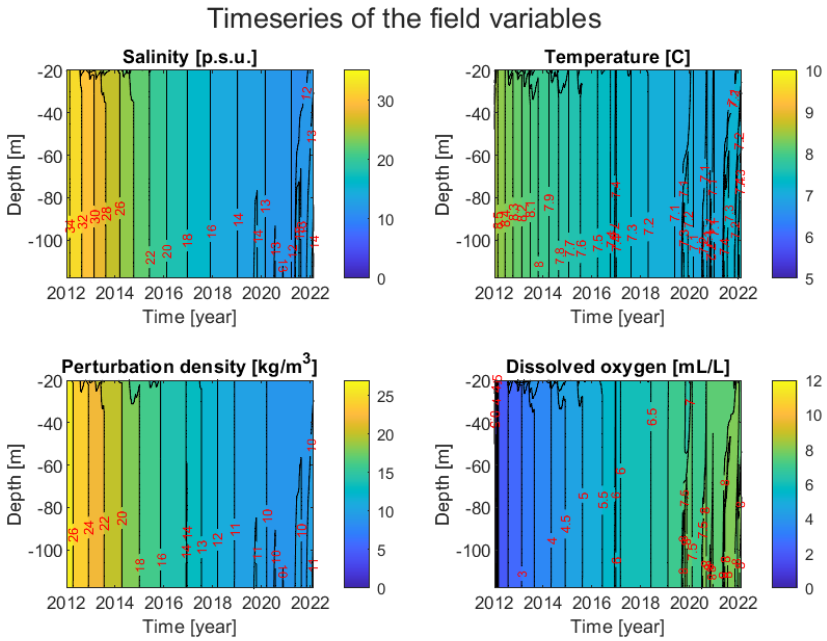

Figure 7.1: The timeseries of the salinity, tempeature, perturbed density and dissolved oxygen concentration in the basin of Haugsværfjorden below 20 m.

$$Q_F \approx 0.52392 \quad \mathrm{m}^3/\mathrm{s} \tag{7.0.0.2}$$

In the model the flux is chosen to be $Q_F = 0.5$ m^3/s for convenience. The fact that $\Delta\rho$ is relatively large and $(\rho_A - \rho_0)$ is relatively small, makes the estimated flux rather large. In fact, with a flux of 0.5 m^3/s it takes only around 11 years to fill the entire basin volume. Thus, the upwelling caused by this flux might be considerable.

In figure 7.1 the timeseries of the evolution of the salinity, temperature, perturbed density and dissolved oxygen concentration in the basin of Haugsværfjoren is presented. In all four panels the isolines are practically vertical through nearly the entire water column below around 20 m. This means that the water below 20 m is very homogeneous and that $\partial\rho/\partial t$ is nearly invariant below 20 m. While the basin waters in the two previous scenarios featured a clear stratification between the intermediate layer and the deeper basin water, this barrier seems to have completely vanished, and the fjord is consisting only of a thin surface layer and a deep underlying homogeneous basin layer.

After 90 days, the patterns of two distinct layers is clearly visible in the profiles in figure 7.2. The surface layer is a thin brackish layer that carries the river runoff out over the sill and the basin water below is a thick homogeneous layer. The intermediate layer seen in the initial conditions is completely vanished. The salinity, temperature and density is quite close to that of the basin water

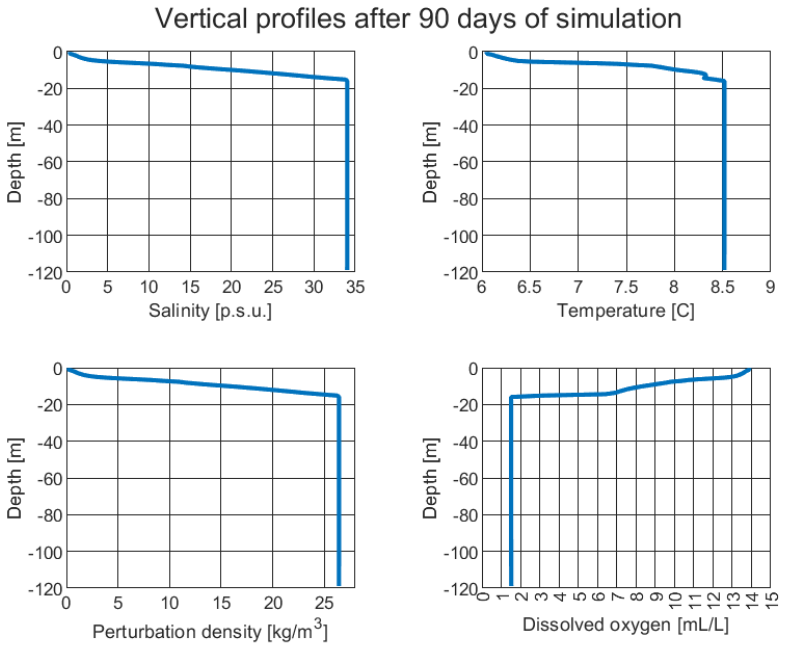

Figure 7.2: The profiles of the four field variables after 90 days of simulation.

in the initial values, seen in figure 4.3, but the dissolved oxygen concentration is definitely nonzero everywhere, which is a considerable difference from the hypoxia seen in both the initial values an the previous scenarios.

In figure 7.3 the profile of the dissolved oxygen field at every 15 days during the first 90 days of the simulation is shown. The dissolved oxygen concentration field reveals the circulatory pattern in the basin which offers an explanation for the homogeneity of the basin water. The fresh water which is discharged at the basin floor has a positive buoyancy and will thus float upwards. This is because the density of the water surrounding the submerged discharge is larger, and specifically the density of the water vertically above the submerged discharge is larger. In other words $\partial\rho/\partial z > 0$ around the submerged fresh water while normally $\partial\rho/\partial z < 0$ through the entire water column. The vertical diffusivity, K_H, is always positive so whether the terms involving K_H in the equations 2.2.0.1 and 2.2.0.2 in subsection 2.2 are positive or not is governed by the gradient $\partial\rho/\partial z$. When $\partial\rho/\partial z > 0$ the turbulent kinetic energy, $q^2/2$, and the product $q^2 l$ increases. This will in turn increase K_H which is proportional to ql, leading to additional increase in the turbulent mixing. This process leads to the mixing of the submerged fresh water and the basin water, which mixes at a rate that is proportional to $\partial\rho/\partial z$. Thus, the effects of positive buoyancy and turbulence will lead to rising water masses that turbulently mixes with the surrounding water.

In the two upper panels of figure 7.3 the rising water masses are clearly visible. In these two panels it can be observed how the upwelling brings the hypoxic

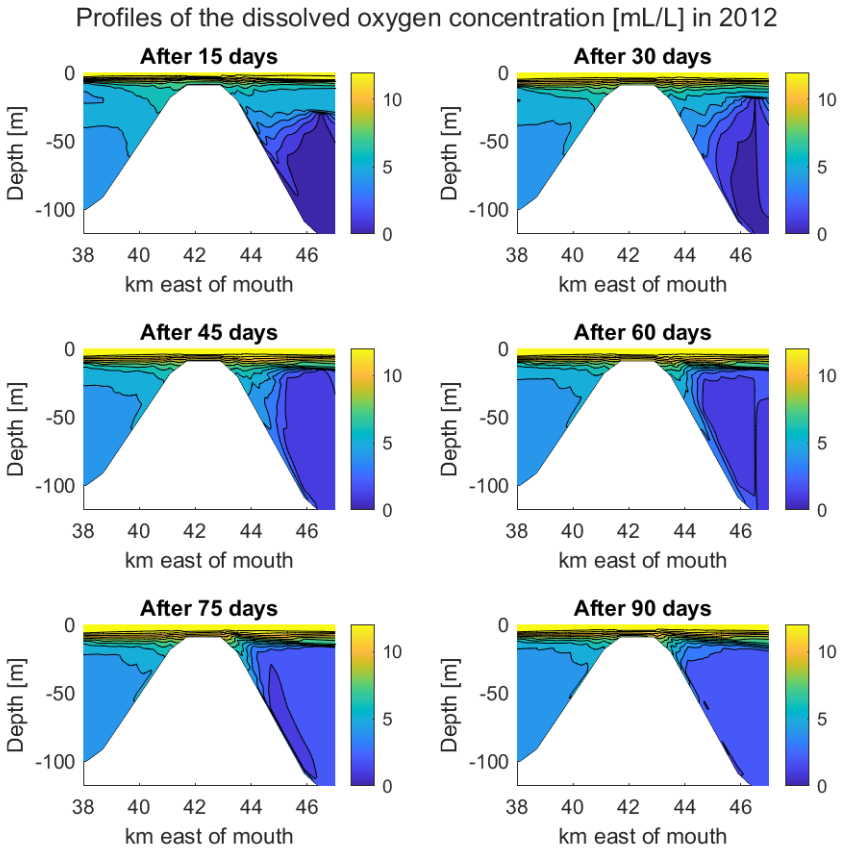

Figure 7.3: The dissolved oxygen concentration field during the first 90 days of the simulation.

basin water higher up in the water column. The water rises in a plume with a large oxygen gradient around it which indicates that the rising water masses and the water masses above it is not completely mixed. In the same two panels a downwelling along the fjord floor can be observed. This is the countercurrent of the rising water masses. This circulatory pattern continues and within the first 90 days the basin water is nearly completely homogeneous due to this circulation which can be seen in the lower panels of figure 7.3.

In figure 7.4 the perturbation density, ρ', at 110 m depth in the basin is seen. Most of the time the water at the basin floor is stagnant, which is characterized by a period of approximtaly constant $\partial\rho/\partial t$ which can also be observed in the four panels of figure 7.1. Contrary to the first two scenarios, in the third scenario there occurs several high density intrusions that sink all the way to the basin floor thus partially renewing the deep basin water. This can be observed in figure 7.1, but is also very clearly visible in figure 7.4 where there are several peaks during the last three years of the simulation due to an increase in the density of the basin water.

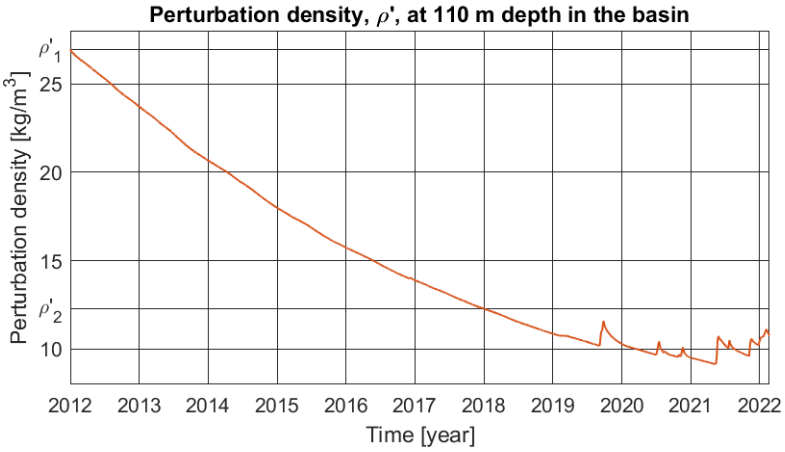

Figure 7.4: The perturbation density, ρ', at 110 m depth in the basin. $\rho'_1 \approx 26.95$ kg/m^3 and $\rho'_2 \approx 12.28$ kg/m^3.

The first high density intrusion that significantly increases the density of the basin water at 110 m depth occurs in the last half of 2019. Prior to this intrusion $\partial\rho/\partial t < 0$ was nearly constant. However, $\partial^2\rho/\partial t^2 > 0$ since $\partial\rho/\partial t$ depends on the difference $\rho_b - \rho_0$ which decreases in time. The perturbed density at the start of the simulation and at the start of 2018 were used to determine the approximate rate of dilution, $\partial\rho/\partial t$, in the basin water.

$$\frac{\partial\rho}{\partial t} \approx -2.445 \text{ kgm}^{-3}\text{yr}^{-1} \tag{7.0.0.3}$$

In the upper panel of figure 7.5 the perturbed density at the sill floor, ρ'_s, is shown. The average value of the density at the sill floor is $\bar{\rho_s} \approx 1011.2$ kg/m^3. At the rate of dilution in equation 7.0.0.3 it takes nearly 7 years before the density at the basin floor, ρ_b, equals $\bar{\rho_s}$, which is a state of equilibrium in the system. It is also not until 2019 that there is an increase in ρ_b which indicates that a high density intrusion has mixed into the water directly above the basin floor. Indeed there occurred a large intrusion at the same time as the increase of ρ_b seen in figure 7.0.0.3. During the intrusion $\rho_s > \bar{\rho_s}$, thus, taken together with the evidence from figure 7.0.0.3 this intrusion event was actually an intrusion that mixed with the deepest basin water. Following the time at which $\rho_b \approx \bar{\rho_s}$ it is expected that in the basin $\partial\rho/\partial t = 0$ on average. Thus, in the stagnation periods $\partial\rho/\partial t < 0$ and during the intrusion events $\partial\rho/\partial t > 0$. The magnitude of $\partial\rho/\partial t$ is greater during high density intrusion events than during stagnation periods, but the two processes are in a balance since the system is in a state of equilibrium.

The boundary conditions in scenario 1 and 3 are the same except for the submerged fresh water source in scenario 3. Thus the conditions over the sill is expected to be quite similar to the ones in scenario 1. The average density at the basin floor in scenario 3 is, as mentioned $\bar{\rho_s} \approx 1011.2$ kg/m^3, which is

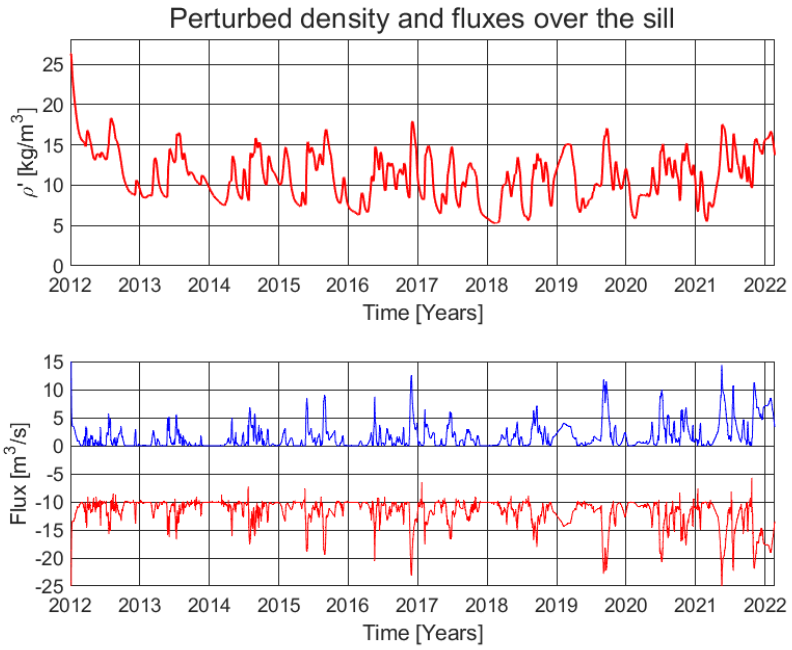

Figure 7.5: The perturbed density at the sill floor and the fluxes over the sill. The blue line shows the eastward flux, Q_{in}, while the red line shows the westward flux, Q_{out}.

very close to the average value in scenario 1 which is $\bar{\rho_s} \approx 1011.32$ kg/m^3. The fluxes, seen in figure 7.5, in the two scenarios are also very similar and many of the intrusion events are recognized in both scenarios, as for example the intrusion event of late 2016 described in chapter 5. One of the significant differences between scenario 1 and scenario 3 will manifest in the ratio ρ_s/ρ_b.

In figure 7.6 it is seen that $\rho_s/\rho_b > 1$ on several occasions, which is a necessary condition in order for the intruding water to sink all the way to the basin floor. For example, in late 2016 the local maximum value of the density at the sill floor at around 1018.4 kg/m^3 occurred, which lead to the ratio increasing significantly to the local maximum value $\rho_s/\rho_b \approx 1.004$ at this time. During this event one of the largest values of Q_{in} during scenario 3 is seen, which attained a maximum value of around $Q_{\text{in}} = 12.5$ m^3/s. The total volume that entered the fjord during this event was around $16.04 \cdot 10^6$ m^3, which is around 9.1 % of the basin volume. However, the density at the basin floor did not increase after this event, which means that the intrusion only mixed with the intermediate layers of the fjord in spite of the fact that $\rho_s/\rho_b > 1$. The turbulent mixing occurring during an intrusion event dilutes the intruding water masses thus possibly stopping the intrusion from reaching the deepest parts of the basin. The turbulent mixing of the intruding water explains how the intrusion in late 2016 did not reach the deepest parts of the basin.

In figure 7.7 the intrusion event in the last half of 2019 is shown in more detail.

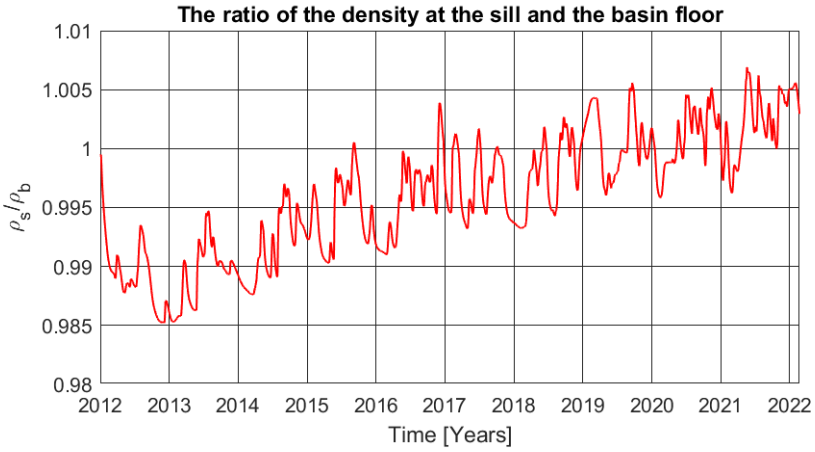

Figure 7.6: The ratio between the density at the sill floor, ρ_s, and the density at the basin floor, ρ_b.

During this event ρ_s is at most slightly more than 0.5 % more dense than ρ_b which can be viewed in figure 7.6. Contrary to the intrusion in the end of 2016, ρ_b increases during this event, thus confirming that the intrusion entered the deepest part of the basin. The increasing density at the basin floor constitutes a negative feedback on the system since ρ_s/ρ_b decreases during the event. Thus, a high density intrusion will eventually stop itself given that the volume of the intrusion is large enough to significantly lower ρ_s/ρ_b, and given that the fluctuations in ρ_s is not the restricting factor. However, from figure 7.7, it is clear that the increase in ρ_b stops while still $\rho_s/\rho_b > 1$. Thus, there seems to be a critical value, q, of ρ_s/ρ_b which decides whether or not a high density intrusion will sink to the basin floor.

It can be observed in figure 7.7 that the increase in ρ_b does not start immediately as $\rho_s/\rho_b > 1$, rather there passes a certain period of time from the high density intrusion starts until ρ_b starts increasing. In fact $\rho_s/\rho_b \approx 1.0052$ around the time ρ_b starts increasing which is at around the date 2019.68. During the intrusion into the basin, ρ_s fluctuates at around a 0.5 % higher density than ρ_b. It can be observed that the intrusion temporarily stops at around the date 2019.71 before it starts again and finally stops just before the date 2019.74. The intruding water uses some amount of time to reach the basin floor as there is around 4 km from the sill to the floor of the basin. Thus, the temporary stop in the intrusion is related to the drop in ρ_s/ρ_b seen around the date 2019.7. The minimum value of this drop is $\rho_s/\rho_b \approx 1.00485$ which leads to the expectation that the critical value is at least larger than this. The intrusion into the basin finally halts at around the date 2019.74 and at this time $\rho_s/\rho_b \approx 1.00477$. Thus it can be expected that $q \approx 1.0048$ is the critical value of ρ_s/ρ_b such that when $\rho_s/\rho_b > q$ the intruding water sinks to the basin floor and otherwise only mixes in the intermediate layer. However, the critical value is likely depending on many factors and will change from event to event. The minimum value of the ratio ρ_s/ρ_b observed during one of the high density intrusion events into the basin floor during scenario 3 is for example $\rho_s/\rho_b \approx 1.0027$, while the average

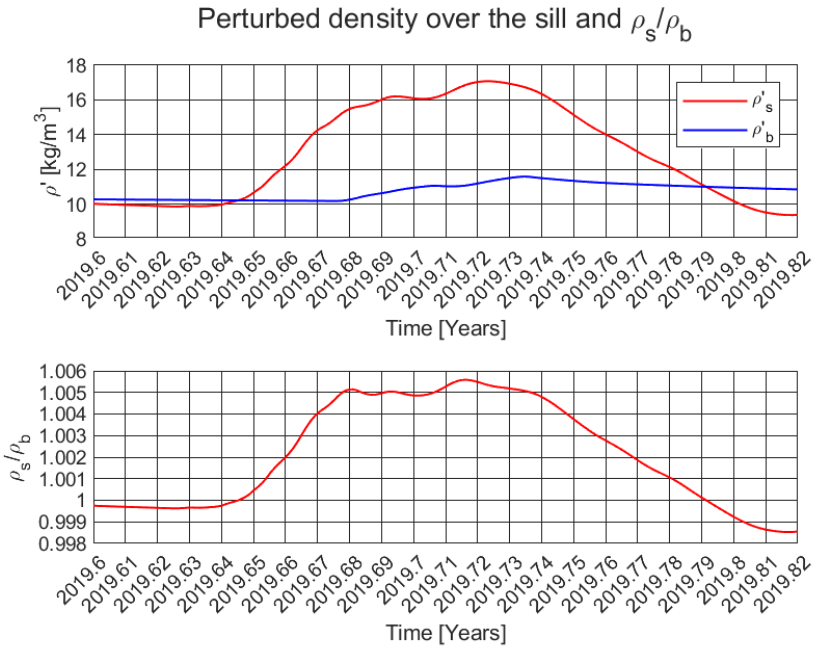

Figure 7.7: In the upper panel the perturbed density at the sill floor and the basin floor is seen. In the lower panel the ρ_s/ρ_b is presented. The time interval is around the high density intrusion in the last half of 2019.

value of this ratio during such high density intrusions is $\rho_s/\rho_b \approx 1.005$. The critical value, q, is probably more precisely defined by a minimum value, but both numbers are useful in at least confirming that the critical value $q > 1$.

The discussed high density intrusion event in the last half of 2019 seems to halt due to the fluctuations in ρ_s rather than an increase in ρ_b leading to $\rho_s/\rho_b < q$. However, the increase in ρ_b might indirectly affect ρ_s since the intrusion displaces the basin water thus forcing water of lower density upwards which in turn leads to an increase in the westward surface current, Q_{out}, that brings brackish water to the sill. The increase in Q_{out} over the sill might stop the lower eastward current, Q_{in}, if it is strong enough. However, the currents over the sill is well within the subcritical regime just as in scenario 1. The maximum Froude number during the simulation is $F_1 \approx 0.0023$ for the upper layer and $F_2 \approx 0.0072$ for the lower layer.

In figure 7.8 and 7.9 the perturbed density, ρ', and the values of K_H during the high density intrusion event in the last half of 2019 is presented, respectively. In the upper left panel of the figures it can be observed how the dense intruding water flows along the basin floor in a thin layer and that the values of K_H is elevated along the front of the intruding water. $K_H > K_{HMIN}$ due to the fresh water discharge at the basin floor as well, but this is a clear evidence of turbulent mixing in the basin water and deep basin water renewal. $K_{HMIN} = 1.4 \cdot 10^{-7}$ is the minimum value of K_H in the model such that $K_H > K_{HMIN}$

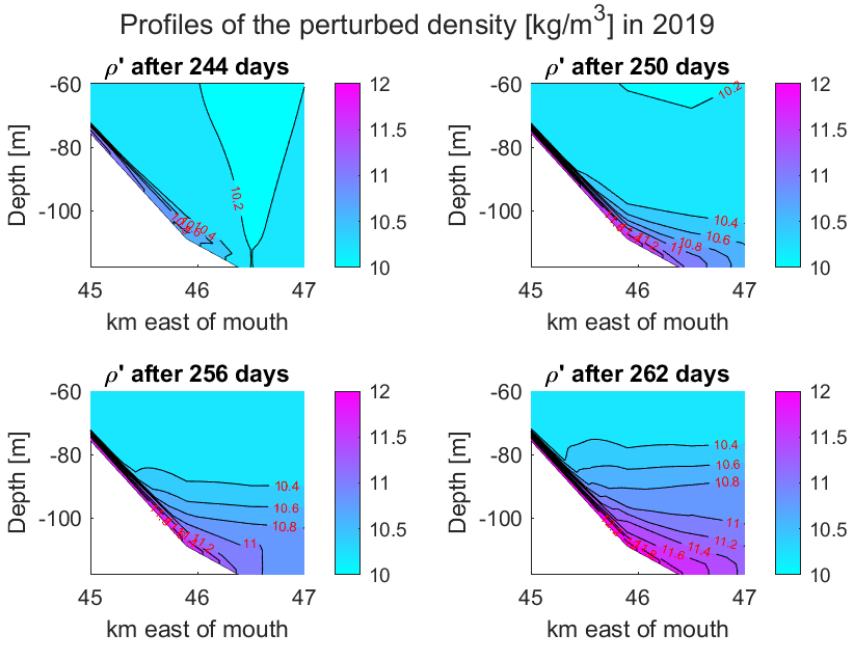

Figure 7.8: Profiles of the perturbed density during the high density intrusion event in the last half of 2019

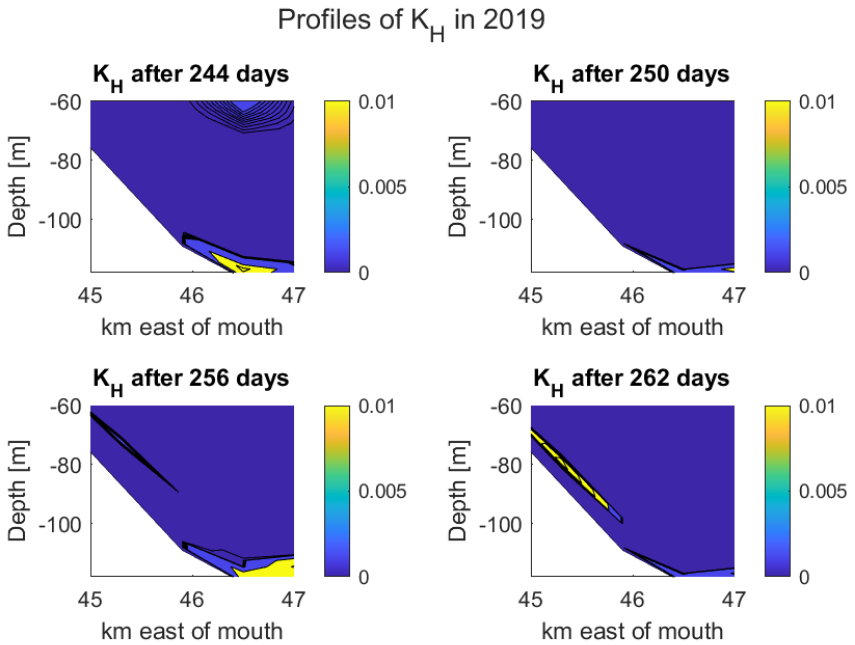

Figure 7.9: Profiles of K_H during the high density intrusion event in the last half of 2019

at all times. The velocity of the intruding water is slightly lower at the basin floor than immediately above the floor due to friction. This causes a wedge of less dense water being trapped underneath the intruding water. At this point $\partial\rho/\partial z > 0$ which induces turbulent mixing of the intruding water and the surrounding basin water. Thus, due to turbulent mixing the intruding water in the upper left panel is just slightly more dense than the basin water even though $\rho_b < \rho_s \approx 1015\text{kg/m}^3$ at the time depicted in figure 7.8.

In the upper right panel it can be seen how the dense intruding water starts filling up the basin floor displacing the deepest basin water. The less dense water in the basin is thus forced upwards which in turn increases the westward surface current by the same amount as the flux of the intruding water masses. In other word, it must be that $Q_{\text{out}} = Q_{\text{in}} + Q_R + Q_F$ where Q_R is the flux of the river discharge and Q_F is the flux of the submerged discharge. As the intruding water fills up the basin floor, ρ_b increases which paves the way for even more dense water to enter the deepest part of the basin, which can clearly be seen in the two lower panels of figure 7.8. Additionally, $K_H > K_{HMIN}$ over the basin floor in all four panels of figure 7.9, which is evidence of the turbulent mixing at the basin floor. Some of this mixing is caused by the intruding water while most of it is likely caused by the submerged fresh water discharge. At most the water intruding the basin floor had a density of slightly greater than 1012 kg/m^3. At this time $\rho_s \approx 1017$ kg/m^3 which is a significant difference. As the duration of the high density intrusion increases this difference might be expected to decrease. However, there will in general always be some turbulent mixing during such events, which means that the density of the water reaching the basin floor is always less than ρ_s during a high density intrusion event.

When comparing the perturbed density at 110 m depth in the basin with the field variables seen in figure 7.4 and 7.1, respectively, it can be observed that the model eventually reaches an equilibrium. From the end of 2019 the perturbed density at 110 m depth in the basin fluctuates around approximately 1010 kg/m^3 as time increases. This pattern can be recognized for the salinity, temperature, perturbed density and dissolved oxygen concentration in figure 7.1, where all three fields fluctuates in a certain range of values at the end of the simulation. The salinity ranges around 12-14 p.s.u., the temperature around 7.2-7.4 C, the perturbed density around 1010-1011 kg/m^3 and the dissolved oxygen concentration around 8 mL/L in the basin water.

The idea behind the submerged fresh water discharge was to reduce the stagnation period of the deepest water by increasing the magnitude of $\partial\rho/\partial t$. This endeavour has indeed succeeded which can be seen by comparing scenario 1 and 3. However, the large $\Delta\rho$ forces the necessary submerged flux to be so large that the fresh water entering from the basin floor itself has ventilated the basin water. The submerged fresh water flux has a dissolved oxygen concentration of 14 mL/L. During the 7 years of stagnation in the deepest basin water the total volume discharged by the submerged fresh water source is roughly $108.9 \cdot 10^6$ m^3, which is approximately 61.5 % of the basin volume. Some of this fresh water originating from the submerged source possibly leaves the fjord during the 7 year period, but arguably such a large discharge will considerably change the characteristics of the basin water.

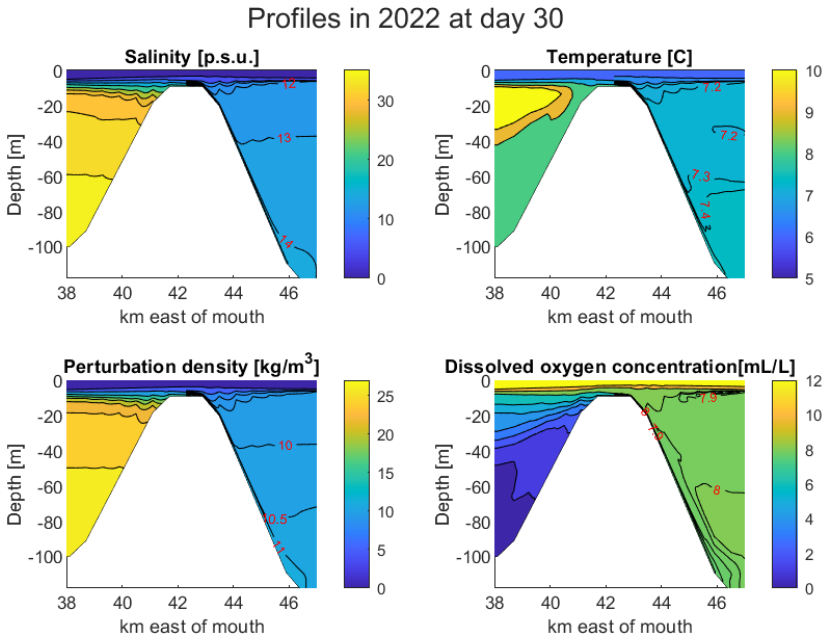

Figure 7.10: Profiles of the salinity, temperature, perturbed density and dissolved oxygen concentration at the end of the simulation during a high density intrusion event.

Indeed, the basin water at the end of the simulation is drastically different from the basin water at the start of the simulation. At the end of the simulation brackish water exclusively constitutes the basin water in Haugsværfjorden, while the basin water at the beginning of the simulation had a salinity in the range of coastal water in the area. The basin water is highly rich in oxygen and dissolved oxygen concentrations exceeding 8 mL/L are observed even at the deepest portion of the basin, which can be seen in figure 7.10. The coastal water is seen in figure 7.10 right outside the sill of Haugsværfjorden. At the instant depicted in figure 7.10 there is a high density intrusion occurring, which can be seen at the 1011 kg/m^3 isopycnal. Nonetheless, the dense coastal water west of the sill is restricted by the sill and cannot generally enter the basin of Haugsværfjorden.

In scenario 1, in the most aggressive approximation, the earliest date a high density intrusion sinking into the deepest portion of the basin water can be expected is during 2037. In scenario 3 this date has been accelerated to 2019. Since regular high density intrusions will only occur when the system is in a state of equilibrium, it must be expected that the basin water in 2037 in the first scenario features similar characteristics as the basin water in scenario 3 in 2019. That is, the frequency of the high density intrusions will not increase significantly before $\rho_b < \bar{\rho_s}$. The same will be the case in scenario 2 in the year 2060, which is the earliest time high density intrusions are expected to sink completely to the basin floor, and occur more frequently. In scenario 2 in

2060 the system will also be in an equilibrium where $\rho_b \approx \bar{\rho_s} \approx 1023.93$ kg/m^3. However, the densities in scenario 2 are significantly greater than in scenario 1 and 3 due to the absence of the river discharge.

In conclusion, the system in scenario 3 reaches the equilibrium state after 7 years of simulation. At this point in time the frequency of high density intrusions increase while the gradient $\partial\rho/\partial t \approx 0$ on average. Disregarding the large amount of dissolved oxygen added to the basin water by the submerged fresh water flux, the high density intrusion events are expected to ventilate the basin water keeping it from turning anoxic. Whether the dissolved oxygen concentrations in the basin would be elevated out of hypoxia is not possible to tell by this study only. However, the dissolved oxygen levels would have to climb above 2 mL/L in the state of equilibrium in order to be classified as well ventilated. Otherwise, the hypoxia would continue. Since the measurements from Haugsværfjorden shows that it is hypoxic below 50 m in the basin, it is reasonable to believe that the basin would continue to be hypoxic even in a state of equilibrium.

Chapter 8

Discussion

In this thesis, a model of the Masfjorden-Haugsværfjorden system has been studied in three different scenarios, focusing particularly on the small threshold fjord Haugsværfjorden. Threshold fjords with shallow sills, like Haugsværfjorden, might have very long stagnation periods and intruding water masses are not likely to displace the entire basin volume during a single high density intrusion event. Thus, the rate of renewal of the basin water is severely restricted in such fjords leading to poor ventilation and hypoxic conditions in the basin water. In order to attempt to establish any conclusion regarding the rate of renewal of the basin water, three scenarios with different conditions have been studied.

In all scenarios, dynamic boundary conditions based on measurements from Sognesjøen has been applied at the outer boundary of the fjord system and the simulation has been run for 10 years. The magnitudes of the river fluxes at the head of Matresfjorden and Haugsværfjorden and the magnitude of the submerged fresh water flux is varied in the study according to the table below.

Scenario no.	Flux of river M	Flux of river H	Submerged discharge
1	155 m^3/s	10 m^3/s	0 m^3/s
2	0 m^3/s	0 m^3/s	0 m^3/s
3	155 m^3/s	10 m^3/s	0.5 m^3/s

The first scenario is a realistic case with dynamic boundary conditions and constant river discharges. During the simulation several intrusion events are observed, however they are relatively small in volume and low in density. Thus, there is no renewal of the deepest basin water during the first 10 years in scenario 1.

The results from scenario 2 reveals that the constant river discharge severely restricts the inflow of water over the sill. In scenario 2, high density intrusions occur periodically in the first half of each year and the largest intrusion had a total volume of nearly half the basin volume. Nevertheless, the density of the

intrusion was less than ρ_b, thus the intrusion did not cause any renewal of the deepest basin water.

In scenario 3, the submerged discharge of fresh water significantly increased the magnitude of $\partial\rho/\partial t$, and high density intrusions caused regular renewal of the basin water after 7 years of simulation. Given enough time, regular renewal was seen to be expected in the two previous scenarios, but in the first scenario the time needed was in the order of decades, while the time required in scenario 2 was in the order of centuries or even millennia. However, the discharge required in order to ensure deep water renewal was vary large and the basin water turned brackish.

In general, the conditions in the model does not favor the renewal of deep basin water. The constant river discharge causes a constant westward flux, $Q_{\text{out}} \geq 10$ m^3, over the sill which restricts the inflow along the sill floor. When a high density intrusion does start, the eastward flux, Q_{in}, increases, which increases Q_{out} by an equal amount. Thus, if Q_{in} grows large enough, the intrusion can potentially choke itself at the sill when Q_{out} grows too large. In this model, the maximum two-way transport capacity over the sill is not achieved, but in reality this might very well occur under the right conditions.

The condition that $\rho_s/\rho_b > 1$ does not alone assure the renewal of deep basin water. In fact, the renewal of deep basin water also depends on the magnitudes of Q_{in} and ρ_s/ρ_b and the duration of the event. For instance in scenario 3 in 2019 it is seen that the renewal of deep water stops while still $Q_{\text{in}} > 7$ m^3/s and $\rho_s/\rho_b > 1.004$. Because the intruding water mixes turbulently with the surrounding basin water upon entering the basin, in order to ensure deep water renewal it must be that $\rho_s/\rho_b > q$, where $q = 1 + \varepsilon$ for $\varepsilon > 0$ is a critical value for ρ_s/ρ_b. The exact value of q most likely depends on the magnitude of Q_{in}, the duration of the intrusion event and also the topography of the fjord floor. If the path from the sill to the basin floor is short q can likely closer to unity, and conversely, q must be larger if the path from the sill to the basin floor is long. Nevertheless, during the intrusion event of 2019 in scenario 3 ρ_s/ρ_b is eventually not large enough to sustain the deep basin water renewal, even though $\rho_s/\rho_b > 1$. However, the intrusion event did not stop right away, but the water renewal shifted to the intermediate layers of the basin.

The result of this study shows that the model of Haugsværfjorden turns entirely brackish before deep basin water renewal occurs. The principle that the basin water is reduced in salinity during stagnation periods applies to reality, but Haugsværfjorden turning brackish in the way seen in the model is deemed unrealistic. The absence of long time series of data measured in Haugsværfjorden restrict some conclusions, but the accessible data from the period 2019-2021 shows a basin water that is not close to turning brackish.

In order to make the model more realistic, it is advisable to reconsider the depth and width of the constriction. According to the maps from Kartverket (2022) the sill into Haugsværfjorden has a maximum depth of more than 25 m which is considerably deeper than the depth of the sill in the model which is at 9 m. A deeper sill will let more dense water flow into the fjord thus increasing the basin

water renewal at earlier dates and most likely maintaining a saline environment in the basin. However, in reality the constriction at the sill is significantly more narrow than in the model. In the model the sill is 600 m wide, while the eastern inlet in Haugsværfjorden is close to 100 m wide, and the cross section at 20 m depth and below is at least less than 50 m wide. A more narrow inlet leads to higher flow velocities which might cause a hydraulically controlled flow over the constriction, and will at least cause more turbulent mixing over the sill. The turbulent mixing and possibly hydraulically controlled flow restricts the inflow of dense water and hence the deep basin water renewal. Nevertheless, considering the hypoxia in Haugsværfjorden seen in the measurements, there is likely a balance in the fjord between the inlet of dense water and restrictions caused by turbulent mixing such that intrusion events are not very large in volume, but perhaps not as rare as was seen in the model. Thus, the basin water remains saline but hypoxic.

Altering the depth and possibly the width of the constriction at the sill can be a natural next step in the study of Haugsværfjorden. Of course, changing these variables will surely bring other sources of error in to the model. However, the goal of these changes would be to more accurately predict the dynamics of Haugsværfjorden.

In conclusion, the model studied in this thesis may not have accurately predicted the deep basin water renewal in Haugsværfjorden and the absolute values of salinity, temperature and dissolved oxygen concentration. Nevertheless, the dynamics of a threshold fjord with a very shallow sill has been described in detail, and the conditions in which deep basin water renewal are seen in the model are deemed realistic in the idealized topography of the model.

Bibliography

Aksnes, D. L., Aure, J., Johansen, P.-O., Johnsen, G. H., and Salvanes, A. G. V. (2019). Multi-decadal warming of atlantic water and associated decline of dissolved oxygen in a deep fjord. *Estuarine, Coastal and Shelf Sciense*.

Berntsen, J. (2004). Users guide for a modesplit σ-coordinate numerical ocean model version 1.0.

Berntsen, J., Darelius, E., and Aksnes, D. L. (2022). Mitigation of oxygen decline in fjords using submerged fresh water.

Blumberg, A. F. and Mellor, G. L. (1987). A description of a three-dimensional coastal ocean circulation model. *American Geophysical Union*.

Cushman-Roisin, B. and Beckers, J.-M. (2011). *Introduction to Geophysical Fluid Dynamics-Physical and Numerical Aspects*. Elsevier Inc.

Darelius, E. (2020). On the effect of climate trends in coastal density on deep water renewal in sill fjords-a statistical approach. *Estuarine, Coastal and Shelf Science*.

Farmer, D. M. and Freeland, H. J. (1983). *The Physical Oceanography of the Fjords*. Pergamon Press, Sidney, Canada.

Kartverket (2022). Norgeskart. *Collected from norgeskart.no*.

Mellor, G. L. and Yamada, T. (1982). Development of a turbulence closure model for geophysical fluid problems. *Review of Geophysics and Space Physics*, 20(4):851–875.

Stigebrandt, A. and Aure, J. (1989). Vertical mixing in basin waters of fjords. *Journal of Physical Oceanography*, 19(7).

Wang, D.-P. (1984). Mutual intrusion of a gravity current and density front formation. *American Meteorological Society*.